Progress in Retinal and Eye Research, *in press*

A reinterpretation of critical flicker-frequency (CFF) data reveals key details about light adaptation and normal and abnormal visual processing

Andrew T. Rider[a], G. Bruce Henning[a] and Andrew Stockman[a]

[a]*UCL Institute of Ophthalmology, 11-43 Bath Street, London EC1V 9EL, England*

Abstract

Our ability to see flicker has an upper frequency limit above which flicker is invisible, known as the "critical flicker frequency" (CFF), that typically grows with light intensity (*I*). The relation between CFF and *I*, the focus of nearly 200 years of research, is roughly logarithmic, *i.e.*, CFF $\propto$ *log(I)*—a relation called the Ferry-Porter law. However, why this law should occur, and how it relates to the underlying physiology, have never been adequately explained. Over the past two decades we have measured CFF in normal observers and in patients with retinal gene defects. Here, we reanalyse and model our data and historical CFF data. Remarkably, CFF-*versus*-*I* functions measured under a wide range of conditions in patients and in normal observers all have broadly similar shapes when plotted in double-logarithmic coordinates, *i.e.*, *log*(CFF)-*versus*-*log*(*I*). Thus, the entire dataset can be characterised by horizontal and vertical logarithmic shifts of a fixed-shape template. Shape invariance can be predicted by a simple model of visual processing built from a sequence of low-pass filters, subtractive feedforward stages and gain adjustment (Rider, Henning & Stockman, 2019). It depends primarily on the numbers of visual processing stages that approach their power-law region at a given intensity and a frequency-independent gain reduction at higher light levels. Counter-intuitively, the CFF-*versus*-*I* relation depends primarily on the gain of the visual response rather than its speed—a conclusion that changes our understanding and interpretation of human flicker perception. The Ferry-Porter "law" is merely an approximation of the shape-invariant template.

Keywords: Visual psychophysics, flicker acuity, critical flicker fusion, CFF, temporal processing, clinical vision, linear systems, gene defects, molecular loss, light adaptation,

GNAT2, *RGS9*, *RPE65*, *GUCA1A*, *GUCY2D*, *OPA1, GRM6, NR2E3*, *KCNV2, LRAT*, *OPN1LW*, *OPN1MW*.

Funding: BBSRC grants numbers BB/1003444/1 and BB/M00211X/1

Contents

1. Introduction

When light flickers above a critical rate (the critical flicker frequency or CFF), the sensation of flicker disappears, and the light appears steady. Our inability to see fast rates of flicker is

exploited in devices that present sequences of images at 24 times per second in the case of film or, more often, at 60 times a second or higher in electronic devices, without our being disturbed by the resulting flicker. The fastest rate of flicker that can be seen under a particular set of conditions is known as the critical flicker frequency (CFF), or sometimes as the temporal acuity limit. The CFF typically increases with light level (e.g., Plateau, 1829), so that we can see substantially higher rates of flicker under bright daytime illumination than at dusk.

The focus of this review is on what the CFF reveals about normal and abnormal visual processing and, particularly, about the biological mechanisms by which we adapt to changes in illumination level and how those mechanisms affect flicker sensitivity. We take advantage of measurements made in normal observers and patients in our laboratory at the UCL Institute of Ophthalmology over the past 20 years and combine them with historical CFF measurements from diverse sources. In the first part of this review, we consider the structure of the CFF versus intensity data, what is constant in that structure, and how it varies in different data sets under different experimental conditions. Later, we relate this structure to a model of light adaptation previously developed to account for the dependence of flicker sensitivity on temporal frequency taken from a variety of historical sources (Rider et al., 2019) and subsequently applied to data obtained from patients (Stockman et al., 2021). The model is described in more detail in Section 4, and is shown schematically in Figure 5**A**, both below.

Research into the CFF has a long tradition that has generated an extensive literature (see Landis, 1954; Simonson and Brožek, 1952). The increase in CFF is almost universally linked to a crucial adaptation mechanism by which the visual system offsets the deleterious effects of increasing mean light levels by shortening its visual integration time; i.e. the speeding up of the visual response as the mean light level increases (e.g., Bills, 1920; Ferry, 1892; Porter, 1902; Pulfrich, 1922; Rogers and Anstis, 1972; Stockman et al., 2006). The speeding up of the visual response with increasing light levels is indeed a crucial mechanism in light adaptation, and it seems intuitive, almost to the point of redundancy, to suggest that faster responses allow us to see higher-frequency flicker. However, our reanalysis and modelling of normal CFF data and the abnormal CFF data from patients reveal that at moderate and higher light levels, the CFF tells us relatively little about the speed of the visual response; rather the CFF depends instead on the number of processing steps in the visual pathway and on the "gain" of the system. We show that the dependence on gain is reflected in normal and abnormal CFF versus

intensity (*I*) functions all of which conform to a common template in double-logarithmic coordinates [*log*(CFF) *versus log*(*I*)]. The implications of this for the interpretation and understanding of CFF data are far reaching. At the outset, we should be clear about what we mean by changes in gain or speed.

We use the term gain in the mathematical sense of a constant value which scales the overall response of the system independent of the stimulus frequency (flicker rate). For example, if we decrease the gain by a factor of 2, the response of the system will be exactly twice as small for the same input, independent of the temporal frequency content of the input. Photopigment bleaching, for example, decreases the response equally at low and high frequencies. "Gain" used thus should not be confused with "gain" as it is often defined in engineering contexts as the ratio of a system's output to its input; this ratio can vary with the temporal frequency of the input.

By "changes in speed", we refer mainly to changes in the speed of the visual response caused by changes in integration time. Shortening the integration time, for example, has the effect of attenuating lower temporal frequencies more than higher frequencies and also of reducing the time to the peak response. Thus, changes in integration time result in frequency-dependent changes in the delay and magnitude of the visual response. Changing integration time is distinct from, for example, changes in a time delay (or latency) that reduce the time to peak response but otherwise leave the response unchanged. These distinct definitions of gain and speed allow us to separate frequency-independent and frequency-dependent differences in sensitivity.

We begin by summarising our methods and describing the CFF data for normal observers.

2. CFF measurements and descriptive models

2.1 Normal CFF measurements

The CFF is usually measured in modern times by presenting observers with a light flickering at or near maximum contrast (*i.e.*, varying smoothly in time back and forth from completely dark to completely light), and then asking them to adjust the rate of flicker to find an upper frequency limit below which the flicker is just visible. In our experiments, the CFF

was measured as a function of the mean illumination using sinusoidal flicker under one of two standard conditions: one favoured flicker detection by long-wavelength-sensitive- (L-) cones and the other detection by short-wavelength-sensitive (S-) cones. In both cases a 4-deg diameter, circular, flickering target was superimposed in the centre of a larger, steady, adapting background of 9-deg diameter. Measurements were made in observers with normal vision and also in patients with abnormal vision. Observers could take as long as needed to adjust the flickering light and find the frequency at which flicker was only just visible. Although relatively large, we have generally found a 4-deg diameter target to be appropriate for both patients with reduced vision and for normal control observers.

To favour L-cone detection, we presented a red (650-nm) flickering target on a blue (481-nm) steady background that was intense enough to saturate the rods (and thus minimize rod detection of the flicker). This combination of target and background also favors L-cone mediated flicker detection since the L-cones are more sensitive than the M-cones to the 650-nm flickering light and less sensitive to the 481-nm steady background (e.g., Stockman and Sharpe, 2000). The presence of the background reduces the flicker contrast at low target radiances and, as we show, alters the CFF, but was necessary to minimize rod contribution in the CFF in patients with low cone sensitivities. Its scotopic luminance of 2.46 $\log_{10}$ scotopic trolands (see Section A1) saturates the rods (e.g., Adelson, 1982; Aguilar and Stiles, 1954).

To favour S-cone detection, we presented a violet (440-nm) flickering target on an orange (620-nm) steady background that was intense enough to adapt the L- and M-cones strongly (and to saturate the rods). This background had very little direct effect on the S-cones, which are insensitive at long wavelengths.

In both cases the CFF measurements were made as a function of the mean target intensity at intervals of approximately 0.3 $\log_{10}$ unit over a range of more than 4.0 $\log_{10}$ units. At each intensity level, the observer was asked to adjust the frequency of flicker to find the frequency at which the flicker was just visible (Figure 1, side panel **C**, illustrates sinusoidal flicker of constant mean intensity and amplitude, and thus of constant contrast; the observers adjust only the frequency of the flicker).

The L-cone and S-cone conditions used here have been used extensively in our clinical work (listed below) and in other flicker experiments (e.g., Stockman et al., 1991; Stockman

and Plummer, 1998; Stockman et al., 2007a). In Figure 1, we have collected the measurements of normal observers from these publications. A central goal of this review is to account for these and other data using a simple explanatory model.

[Insert Figure 1 about here]

In the main panels **A** and **B** of Figure 1 the CFF (in cycles per second or hertz, Hz) is plotted as a function of the logarithm of the average intensity [(radiance)—$\log_{10}$ quanta s^{-1} deg^{-2}]. The L-cone CFF measurements in Figure 1**A** were made in 21 normal observers (mean age 33 years, range 21 to 65), and the data from each observer are shown as coloured. The means taken over all the observers are plotted as black circles and the white error bars show two standard errors of the mean (±2SEM) across observers. S-cone CFF measurements (Figure 1**B**) were made in 12 observers (mean age, 40 years, range 23-65) and the individual S-cone data are again plotted as coloured symbols with means plotted as black circles (error bars are again ±2SEM). (The CFFs of the 10 observers in whom both L- and S-cone measurements were made are distinguished in both panels by symbols with thin black outlines.)

The general forms of the L-cone and S-cone CFF functions plotted in Figure 1 are consistent across observers. The L-cone functions rise from low target radiances and follow an approximately straight-line on these coordinates before becoming much shallower above about 9.5 $\log_{10}$ quanta s^{-1} deg^{-2}. Under these conditions, the L-cone CFF rarely rises above about 45 Hz, which is lower than the CFFs typically obtained using white light (see Figure 3**A**, below). The S-cone functions also rise from low target radiances and also follow a straight line before approaching a plateau at about 9 $\log_{10}$ quanta s^{-1} deg^{-2}. Unlike the L-cone data, however, there is a subsequent rise above 10 $\log_{10}$ quanta s^{-1} deg^{-2}. Stockman & Plummer (1998) showed by varying target wavelength that this later rise has an M-cone spectral sensitivity and is therefore likely to reflect flicker detection by M-cones (see their figure 4).

2.2 Ferry-Porter law

A well-established description of CFF data is that they grow in proportion to the logarithm of light intensity (*I*), so that plots of CFF versus log *I*, as in Figure 1, follow a straight line which we indicate by the black lines in Figures 1**A** and 1**B**. This property is known as the Ferry-Porter

law (Ferry, 1892; Porter, 1902), and, indeed, many experiments over many years confirm that this relation, or a close approximation to it, holds over a substantial range of light intensities (e.g., Corwin and Dunlap, 1987; Hecht and Verrijp, 1933b; Ives, 1912; Tyler and Hamer, 1990, 1993). Moreover, the law holds, with different slopes, across different stimulus parameters, such as changes in target size, retinal eccentricity, and wavelength (e.g., Ives, 1912; Landis, 1954; Simonson and Brožek, 1952). Remarkably, too, the Ferry-Porter law is also approximately true across a variety of clinical visual defects, some of which markedly reduce both the CFF and the slope of the line. (For convenience, we shall call the slope of the best fitting line the "Ferry-Porter or FP" slope.)

Our L- and S-cone data for normal observers are clearly well described by the Ferry-Porter law. The black lines in Figures 1**A** and 1**B** with slopes of 8.73 and 7.42 Hz per decade, respectively, have been fitted to the mean CFF data. As can be seen, the Ferry-Porter law holds from about 7 to 9 or 10 $\log_{10}$ quanta s^{-1} deg^{-2} for the L-cone data and from about 7 to 9 $\log_{10}$ quanta s^{-1} deg^{-2} for S-cones—more than a factor of 100 times increase in light intensity. For the individual L-cone data, the best-fitting FP-slopes (not shown) vary from 6.33 to 10.81 Hz per decade with a mean of 8.60 with a standard deviation of 1.21 Hz per decade. For the individual S-cone data, the best-fitting FP-slopes (not shown) vary from 5.41 to 9.06 Hz per decade with a mean of 6.91 and a standard deviation of 1.21 Hz per decade. The difference in FP-slopes between the L- and S-cone CFFs was highly significant (two-sided t-test: t=3.87, P<0.001). Traditionally, the shallower S-cone FP-slope is interpreted as showing that the S-cones and their pathways are slower than the L-cones and their pathways.

Linear relations are compelling, and the Ferry-Porter law provides a plausible description of the dependence of CFF on *I*. However, it does not suggest an easy or coherent explanation of why the relation is logarithmic (*i.e.*, why CFF versus intensity functions should follow straight lines in the semi-logarithmic co-ordinates of Figure 1). Nor does it suggest why the Ferry-Porter slope varies across observers and conditions.

One intuitive interpretation of the Ferry-Porter slope has been that its steepness somehow reflects the “speed” of the underlying visual processing, with steeper slopes correlating with greater speed-of-processing. This is exemplified by Tyler & Hamer (1990) and Hamer & Tyler (1992), who suggested that the steeper slopes found in peripheral vision imply that peripheral cones are faster than foveal ones, and by Hamer & Tyler (1992), who

suggested that steeper slopes found with 552-nm flickering lights than with 642-nm lights imply that the M-cones and their pathways are faster than L-cones and their pathways. Our analysis of CFF functions suggests an alternative interpretation.

2.3 Log-log shape invariance

A different description of the relation between CFF and *I* is that it follows a power-law (Collins, 1956; Piéron, 1922; Raninen et al., 1991), so that it is a plot of *log* CFF versus *log I* that should follow a straight line (rather than CFF versus *log I*). Using the same symbols as in Figure 1, we replot the individual CFF data in Figure 2**A** in double logarithmic co-ordinates (CFF on a logarithmic axis vs log average radiance) having first separately aligned the L-cone and S-cone CFF data by shifting them vertically and horizontally. [The horizontal and vertical shifts are shown in Figure 11, below, as red (L-cone) and blue (S-cone) crosses; see Appendix A4 for details of the alignment process.] Pure horizontal shifts are consistent with changes in the effectiveness of the light, a good example of which would be a change in quantal sensitivity caused by pre-receptoral opacities. A pure vertical shift would correspond to a constant multiplicative change in CFF at all light levels, but it is difficult to envisage a biological mechanism that would cause such a shift. As discussed below, gain changes after photon absorption are consistent with combinations of vertical and horizontal shifts.

It is readily apparent that the functions do not conform to straight lines as they would if they were consistent with a power-law, but they do follow consistent shapes or templates in the double logarithmic co-ordinates. We extracted L-cone and S-cone template functions using Locally Estimated Scatterplot Smoothing (LOESS) (Cleveland, 1979). The smoothed templates are shown by the solid white (L-cone) and solid black (S-cone) lines in Figure 2**A.**

[Insert Figure 2 about here]

A second stage of alignment is shown in Figure 2**B** in which the L- and S-cone templates have been aligned with each other and then the data shifted and replotted accordingly. As can be seen, there is excellent agreement between the two datasets until the S-cone pathways begin to plateau above 9.2 $\log_{10}$ quanta s^{-1} deg^{-2}.

The template shapes are curved over most of their range. Nevertheless, some portions approximate straight lines and are therefore consistent with a power-law (Collins, 1956; Piéron, 1922), but the ranges over which this occurs (approximately 2.0 and 1.5 $\log_{10}$ units for the L- and S-cone CFFs, respectively) are smaller than the ranges over which the Ferry-Porter law holds.

Later, in the Discussion, we present a model (Rider et al., 2019; Stockman et al., 2021) that can account both for the template shape and for the aligning shifts.

For now, however, the important conclusion is the empirical finding that in double-logarithmic coordinates the L-cone and S-cone CFF functions of individual observers conform to a single template over 3 decades of intensity with the individual differences being consistent with vertical and/or horizontal shifts of the individual data sets.

3. Historical CFF measurements

In Figures 2**A** and 2**B**, we showed that the L- and S-cone CFF data have approximately invariant shapes when plotted in double-logarithmic coordinates. But how general is this finding? Does the same invariant shape apply under other stimulus conditions? To investigate that question, we extracted historical CFF data from several publications (de Lange, 1958; Giorgi, 1963; Hamer and Tyler, 1992; Hecht and Shlaer, 1936; Hecht and Verrijp, 1933a; Ives, 1912; Pokorny and Smith, 1972; Porter, 1902). Table 1 summarises the stimulus conditions used in these studies (please refer to the original papers for more information). Pokorny & Smith's observers included 7 deuteranopic and 4 protanopic observers; otherwise, the observers were likely to have normal colour vision. Typically, the method of adjustment or method of limits was used, although Hamer and Tyler (1992) use 1-s cosine-windowed flicker bursts to mitigate against adaptation to flicker. De Lange states that he limited viewing to 5 seconds "to prevent local adaptation to small variations of brightness," but it is not clear from the descriptions in the methods of the other studies whether any steps were taken to mitigate this. However, in any case it has been shown that at the CFF the effect of flicker adaptation is likely to be relatively small (Ginsburg, 1966).

Study	Type of light	Target Size (deg)	Retinal Position	Background diam. (deg)	Observers
Porter (1902)	White light	Not given	Probably central	None	1
Ives (1912)	White or 480 to 650 nm	rectangular 5.2 by 8.6	Probably central	None	1
Hecht & Verrijp (1933)	White light	2 diam.	Central	10	2
Hecht & Shlaer (1936)	From 450 to 670 nm	19 diam.	Central	35	2
De Lange (1958)	White light	2 diam.	Central	60	1
Giorgi (1963)	From 450 to 660 nm	1.66 diam.	Central	7	3
Pokorny & Smith (1972)	Lights of 580 nm	1 diam.	Central	None	14
Hamer & Tyler (1992)	Lights of 555 or 642 nm	0.5 or 5.7 diam.	Central or 35 deg eccentricity	Hemispheric white surround	4

Table 1: Details of the historical CFF studies

The historical CFF data are reproduced in Figure 3**A** on the traditional semi-logarithmic co-ordinates (such that the Ferry-Porter law would appear as a straight line). The symbols noted in the key correspond to CFF data for individual observers obtained from the eight studies. Symbols of the same type but different colour correspond to variations in stimulus wavelength within the same observer. The intensity scale (luminance in $\log_{10}$ trolands, Td) is approximate, since in some studies the intensity calibrations are unclear or missing. To aid comparison and emphasise the different Ferry-Porter slopes in Figure 3**A**, we have horizontally aligned the CFF data at 20 Hz. The luminance scale is correct for Hecht and Shlaer's (1936) data shown as triangles. Much of the CFF data below about 0 $\log_{10}$ Td in these historical studies is likely to reflect rod activity. This can be seen clearly in Hecht and Shlaer's data (where the colours of the triangular symbols are used to suggest the wavelength of the stimulus). Note that below 0 $\log_{10}$ Td their CFF data (aligned in the photopic region) increasingly extend to lower luminances as the wavelength decreases (blue to violet symbols) and the rods become more and more sensitive relative to cones (e.g., Wald, 1945).

[Insert Figure 3 about here]

Above 1.5 $\log_{10}$ Td, the CFF functions in Figure 3**A** fan out with different slopes. For each observer, the Ferry-Porter law provides a plausible description of the rising slope, which illustrates why the law has been generally accepted. Nevertheless, plotted in these coordinates, there are substantial differences between the functions. First, the Ferry-Porter slopes vary from about 10 to 20 Hz per log unit of intensity. Second, the limiting plateaux at higher luminances vary in both horizontal (*log I*) and vertical (CFF) position with some data showing little evidence for any plateau.

The crucial next question is whether these disparate data also conform to an invariant shape in double-logarithmic coordinates. We realigned the data in double logarithmic coordinates and replotted them in Figure 3**B** first removing data points below 0.5 $\log_{10}$ Tds that are most likely rod-mediated. Now the highly disparate functions of Figure 3**A** conform closely to a single template shape. The solid white line in Figure 3**B** shows the template shape for the aligned data again derived using LOESS. The agreement is quite remarkable (with a root mean squared error of 0.024 $\log_{10}$ Hz); not only have the effects of different wavelengths, target size, retinal eccentricity, and signal duration disappeared but so too have the differences among the individual observers in sensitivity, optical absorption, and criterion placement—the CFF data follow, and with very little variability, the same function in double logarithmic coordinates. This is not to say that the above factors do not significantly affect the CFF, but, as can be seen, their effects are largely accounted for by shifts in double-logarithmic co-ordinates.

[Insert Figure 4 about here]

In Figure 4, we align the historical data with the L-cone and S-cone CFF data from Figure 2, shown as grey, pink and violet symbols, respectively, and also plot the templates for the historical data (black-white dashed line), L-cone data (white line) and S-cone data (black line). (The three templates are tabulated in this alignment in Table B3 in the Appendix.) There are two regions where these templates diverge.

The deviation of the S-cone template from the historical and L-cone templates in Figure 4 above about 3 $\log_{10}$ Td and shaded in pale green, are, as noted above, the result of S-cone saturation and, at the highest levels, of the detection of the 440-nm target by M-cones (e.g., Stockman and Plummer, 1998). The deviations between the historical template and the L- and

S-cone templates below about 1 $\log_{10}$ Td and shaded in khaki are caused by our use of steady backgrounds to eliminate rod contributions in the case of L-cone CFFs and to isolate the S-cone response from the L- and M-cone and rod responses in the case of S-cone CFFs. These backgrounds, necessary to eliminate unwanted responses from rods or other cone types, have the additional effect of reducing flicker contrast at lower light levels. The backgrounds thus limit the lowest level of adaptation that can be reached in our experiments. This limitation is not found in most of the historical experiments.

To confirm that the 481-nm background causes the differences between the historical and L-cone templates, we remeasured the L-cone CFF in 5 observers using the same 650-nm target but crucially without the background with and without a rod bleach. Bleaching rods and making measurement during the cone plateau is one way to ensure that only cones mediate detection (Kohlrausch, 1922). The aligned CFF data, which are shown in Figure 4 as cyan symbols with black outlines, are consistent with the historical template, and thus also with the historical CFF data that we assumed to be cone-driven.

As discussed later, we can account for the differences between the L-cone data with and without the 481-nm background and for the differences between the historical and L-cone templates by assuming that the background prevents full dark adaptation, thus setting a lower limit to the speed of visual processing.

Dark-adapted rods can tonically suppress cone signals such that cone sensitivity improves as rods become light adapted, an effect referred to as suppressive rod- cone interaction (SRCI) (Alexander and Fishman, 1984; Coletta and Adams, 1984; Frumkes and Eysteinsson, 1988; Goldberg et al., 1983). However, while SRCI may play some role in determining the shapes of the CFFs by changing the overall gain, it cannot explain the differences highlighted in khaki in Figure 4, since it predicts that sensitivity should increase on the 481-nm background, not decrease.

While there are remarkable similarities between the $\log_{10}$ CFF versus $\log_{10}$ *I* relations under very different conditions, this finding, like the Ferry-Porter law, is so far largely descriptive. In order to explain the empirically obtained CFF template shapes, we next analyse them with reference to simple models of vision and visual processing.

4. Models of temporal processing applied to the CFF

4.1 The Ferry-Porter law and shape invariance

As discussed in section 2.2, the relation between CFF and *log*(*I*) has frequently been shown to follow a straight line over an extended range of *log*(*I*) in accordance with the Ferry-Porter law, but the reason for this and for the differences in the slopes of the Ferry-Porter lines have never been convincingly explained. By examining a range of CFF datasets measured in normal observers we have found that, plotted in double-logarithmic coordinates [*log*(CFF) versus *log*(*I*)], almost the entire dataset can be summarised by a shape-invariant template shifted appropriately along the *log*(CFF) and/or the *log*(*I*) axes. Such shape-invariance should, in fact, be expected over those ranges of *I* for which the Ferry-Porter law holds. This can be illustrated mathematically.

The Ferry-Porter law can be written:

$$\mathrm{CFF} = m \times \left(\log_{10}\left(I\right) - c\right), \qquad (1)$$

where *m* is the Ferry-Porter slope and *c* is the log intensity at which the CFF would fall to zero. Thus, the CFF is a straight-line function of $log_{10}(I)$ with a slope of *m* (Hz per decade). If we take the logarithm of both sides of this equation (as if we were plotting the function in double-logarithmic coordinates), we get:

$$\log_{10}\left(\mathrm{CFF}\right) = \log_{10}\left(m\right) + \log_{10}\left[\log_{10}(I) - c\right]. \qquad (2)$$

In Equation 2, $\log_{10}(\mathrm{CFF})$ is a logarithmic function of $\log_{10}(I)$ that can be shifted horizontally and vertically in double-logarithmic coordinates by varying *c* and $\log_{10}(m)$, respectively. Consequently, when the Ferry-Porter law holds, $log_{10}(\mathrm{CFF})$ *versus* $log_{10}(I)$ functions should be alignable—with appropriate horizontal and vertical shifts. As discussed above, most of the data presented so far approximate the Ferry-Porter law over significant ranges of $log_{10}\ I$. Consequently, the templates also approximate logarithmic functions over the same ranges when plotted in double-logarithmic coordinates (Figure 4).

Adherence to the Ferry-Porter law implies a common template in double-logarithmic co-ordinates. However, the converse is not true—a common template does not necessarily imply the Ferry-Porter law and the template of Figure 4 summarises the data well beyond

the range over which the Ferry-Porter law holds. The important next question is what causes compliance with the Ferry-Porter law, or more broadly what underlies the template shapes seen in Figure 4? Can we explain the template shapes by applying standard models?

4.2 Leaky integrators, the power-law and the Ferry-Porter law

A by now traditional way of understanding temporal processing has been to assume that visual performance, particularly at higher frequencies, is limited by the speeds of a critical number of sequential steps, each of which can be modelled as a low-pass (LP) filter, also known as a "leaky integrator" (see, for review, Shapley, 2009). The amplitude sensitivity, *S(f)*, of such a sequence of *n* identical LP filters is given by:

$$S(f) = \frac{G}{(2\pi)^n \left(f^2 + f_c^{\,2}\right)^{n/2}}, \qquad (3)$$

where f is the frequency, f_c is the corner frequency of the n identical filters, both in Hz; G is the gain. Corner frequencies are a useful way of characterising low-pass stages in a response versus frequency plot since the corner frequency is the frequency above which a low-pass stage significantly reduces sensitivity. Thus, the corner frequency, f_c, is related to the speed of processing of the filters. The higher f_c the "faster" the filter. At high frequencies, where $f >> f_c$, Equation 3 simplifies to a power law:

$$S(f) \approx \frac{G}{(2\pi f)^n}. \qquad (4)$$

To model the CFF, we need to link it explicitly to amplitude sensitivity, *S(f)*. To do that we assume that flicker is visible if the internal response, *S(f)*, exceeds some fixed threshold, which we can set to 1 without loss of generality. The internal response amplitude is equal to the amplitude of the flicker, *A*, multiplied by the sensitivity, *S*. In most CFF experiments, the contrast of the sinusoidally flickering stimulus is kept constant at or near 100%, so that *A* is very nearly equal to *I*. Thus, when *f* is equal to the CFF, and the internal response, *S*, is at the threshold, $I \times S(f)$ must equal 1, so that *S(CFF)* = 1/*I*. Subsitituting 1/*I* for *S(f)* in Equation 4 and rearranging, we get:

$$\mathrm{CFF} \approx \frac{\sqrt[n]{GI}}{2\pi}, \tag{5}$$

where *f* is now the CFF. Taking logs of both sides, and rearranging again we get:

$$\log(\mathrm{CFF}) \approx \frac{1}{n}\log(I) + h, \tag{6}$$

where *h* is a constant equal to $1/n \log(G) - \log(2\pi)$. Thus, a plot of *log*(CFF) versus *log*(*I*) is a straight line function in double-logarithmic space with a slope of 1/*n* where *n* is the number of low-pass filters, but will shift vertically in *log*(CFF) depending on the gain, *G*. As noted above, parts of the CFF template functions plotted in double-logarithmic coordinates approximate to straight lines over limited ranges before the functions start to asymptote at higher mean intensities. The slopes in those ranges are approximately 1/6 or 1/7, consistent with *n* = 6 or 7 low-pass stages, and thus are similar to values from previous studies that suggested a power law relation between CFF and *I* rather than the Ferry-Porter law (Collins, 1956; Piéron, 1922; Raninen et al., 1991).

An important simplifying assumption in deriving Equation 6 is that the CFF is always much higher than f_c so that the latter can be neglected (as in Equation 4). However, although the visual system approaches the power law region where $f >> f_c$ and is thus characterized by Equation 4, it probably never reaches that region at any light level below the CFF (see Figure 12 of Rider et al., 2019). Consequently, the power law of Equation 4 can only be an approximation since the CFF will depend on f_c as in Equation 3.

Another approach has been to apply Equation 3 directly to the CFF data to account for the Ferry-Porter law (Hamer and Tyler, 1992; Tyler and Hamer, 1990). And, consistent with this approach, the decline in sensitivity of an *n*-stage filter with a fixed f_c approximates an exponential function rather than a power law over a range of frequencies (Hamer and Tyler, 1992; Rider et al., 2019; Stockman et al., 2021; Tyler and Hamer, 1990); *i.e., log* sensitivity plotted as a function of frequency is a straight line, the slope of which varies according to the number of stages and their corner frequencies. Hamer and Tyler (1992) showed that their CFF data are consistent with the Ferry-Porter law and with a 9-stage filter (see their figure 8a). Thus, they equate the exponential decline of flicker sensitivity with frequency to the logarithmic increase of CFF with light intensity, both of which are straight lines in semi-

logarithmic coordinates. A serious concern with this type of model, however, is that it ignores any form of light adaption since it requires that the f_c of each of the 9 stages and the overall gain both to be independent of light level. Hamer and Tyler justify this assumption by appealing to Kelly's notion of "high-frequency linearity" (Kelly, 1961) in which light adaptation leaves the CFF unchanged and the entire CFF function is merely an extrapolation of the response at low light levels. On this view, the CFF represents the "unadapted" response of the visual system, and changes in the Ferry-Porter slope correspond to changes in the unadapted speed. Elsewhere, however, we have shown that high-frequency linearity is at best a rough approximation and certainly does not hold over the full range of light levels over which CFFs are measured; not only does the f_c of the majority of LP stages vary substantially with light level but so too does the overall gain (Rider et al., 2019; Stockman et al., 2006). Moreover, in terms of explaining the form of the CFF functions, there is no clear theoretical basis for why high-frequency linearity should hold, so invoking it to explain CFFs raises as many questions as it answers.

In the next section, we employ a more realistic model to account for the CFF data in which both f_c and gain depend on light intensity. The model was previously developed to account for historical flicker-sensitivity data (Rider et al., 2019) and can predict how flicker sensitivity varies as a function of frequency across light levels for normal observers and clinical patients (Stockman et al., 2021) as well as predicting the CFF data.

4.3 Light adaptation and the CFF

The visual system regulates its sensitivity as light levels change by processes of light adaptation or sensitivity regulation. Such processes are necessary because the human visual system must operate effectively over light levels that vary by as much as 10^{12} despite neurons' in the visual pathway having response ranges that are limited to 10^3 or less (e.g., Barlow and Levick, 1976; Shapley and Enroth-Cugell, 1984). Perhaps the most important sensitivity regulating process at photopic (cone-mediated) levels is the speeding up of the visual response as the light level increases (Bills, 1920; Ferry, 1892; Porter, 1902; Pulfrich, 1922; Rogers and Anstis, 1972; Stockman et al., 2006). This speeding up reduces the integration time of the system, so decreasing the system's response to mean light level and thus preventing its being overwhelmed as the light level rises. A second important process of sensitivity

regulation is the control of overall system gain, such that the gain decreases as the light level rises and increases as it falls. Gain changes, which adjust the sensitivity equally across all frequencies, seem to act mainly at higher mean light levels (see Rider et al., 2019).

One way to fully understand the dependence of CFF on light level is to apply a model that explicitly incorporates the effects of light adaptation. We recently developed such a model to account for the way temporal contrast-sensitivity functions (TCSFs) change with mean light level. TCSFs are measures of the dependence of flicker sensitivity jointly on flicker contrast and on flicker frequency for different mean intensity levels. Thus, the CFF is a section through a set of TCSFs at a constant contrast, usually chosen to be close to 100%. The TCSF model incorporates intensity-dependent changes both in overall gain and in the processing speed of a cascade of LP-stages (Rider et al., 2019; Stockman et al., 2021). Here, we apply this model to the CFF data.

The model is shown schematically in Figure 5**A**. It is made up of an overall gain control, *G*, a sequence of *n* = 6 LP-stages, labelled [1] to [6], with 2 feedforward stages of subtractive inhibition (each with an additional LP-stage [A] or [B] in the feedforward loop and each with a gain control, *k*, that determines the strength of inhibition).

[Insert Figure 5 about here]

The corner frequencies of four of the LP-stages [1] to [4] as well as the two LP-stages [A] and [B] in the feedforward loops (f_c in the equations below), increase with increasing light level thus causing a speeding up of the visual response. We retain the simplicity that all the variable corner frequencies change together. (We shall see that the slope of the CFF function does not, in fact, depend on this mechanism for changing the speed of the visual response; nor can the corner frequencies be inferred from the FP slope.) The two other LP-filters [5] and [6] have fixed corner frequencies (f_{cL}). The strength of the feedforward inhibition can vary from 0 to 1. Both the speeding up and subtractive inhibition reduce sensitivity to low frequencies as well as shaping the temporal response. The changes in TCSF between light levels can be largely modelled by changes in just two variables: the speed of the visual response (changes in f_c) and changes in gain, *G* (Rider et al., 2019). We now apply this model to predict how CFF varies with *I*.

The model defines amplitude sensitivity, *S(f)*, to different frequencies of flicker, *f*, at a fixed light level, *I*, as,

$$S(f) = G(I)\frac{\left(f^2 + \left((1-k)f_c(I)\right)^2\right)}{(2\pi)^6\left(f^2 + f_c(I)^2\right)^3\left(f^2 + {f_{cL}}^2\right)}, \quad (7)$$

where the strength of inhibition, k, and two corner frequencies, f_{cL}, are both fixed, while the gain, $G(I)$, and the variable corner frequency, $f_c(I)$, vary with light level. $S(f)$ predicts the TCSF at a given light level (Rider et al., 2019).

In developing the model, we found:

(i) that f_{cL} and k could be fixed across I, and further,

(ii) that the gain, $G(I)$, is approximately constant at low light intensities, and inversely proportional to the mean intensity at high levels. The characteristics of $G(I)$ could be well described by the function:

$$G(I) = \frac{G_{max} I_{50}}{I + I_{50}}, \quad (8)$$

where G_{max} is the maximum gain in the dark and I_{50} is the half-gain intensity (*i.e.*, the light level that reduces the gain to 50% of its maximum).

(iii) The variable corner frequencies, f_c, follow a power law of I at low to moderate levels before reaching a plateau and are thus captured by:

$$f_c(I) = a\left(\frac{I \times I_{50}}{I + I_{50}}\right)^b, \quad (9)$$

where a and b are constants. Equation 9 is a slightly modified version of the original equation added to avoid a slight discontinuity in the CFF predictions (see Appendix C2 for more details). I_{50} appears in both Equation 8 (for the gain) and 9 (for the variable corner frequencies), which implies that the speeding of the response and the reduction in gain are yoked, so that the gain reduction takes over when the speed of processing is no longer accelerating, perhaps due to inherent limits on how fast some process can be driven, but this may not be the case. The link does, however, reduce the number of free parameters and improves the robustness of the fits.

In our previous work, we estimated these parameters: f_{cL} and k, were 30.9 Hz and 0.80, respectively, the gain parameters were $\log_{10} G_{max}$ = 12.69 and $\log_{10} I_{50}$ = 3.13 $\log_{10}$ Td, and the parameters that determine the corner frequency (Equation 9) were a = 4.07 and b = 0.210 (Rider et al., 2019). The dashed black lines in three righthand panels of Figure 5 are replotted from Rider *et al.* (2019) and show f_{cL} and f_c (in panel **B**), G (in panel **C**) and k (in panel **D**) each as a function of $\log_{10}(I)$. The red curves are the modified versions that we fit to the historic CFF data, see below.

As noted, these equations were developed to account for the way sensitivity as a function of frequency (TCSF) varies with I measured under variable but similar conditions—typically, colour normal observers viewing white flickering lights. As above with Equation 4, we need to set $S(f)$=1/I in Equation 7 and rearrange the equation to get frequency as a function of I. However, Equation 7 is more complicated than Equation 4.

To model the effects of light adaptation on the CFF, we must solve Equation 7 to give f in terms of I and the other parameters. This is a non-trivial problem, so it is understandable why earlier workers have tried to simplify the problem by ignoring I. However, since f only appears in Equation 7 as f^2, the equation can be rewritten as a fourth order polynomial in f^2. We found a solution for this equation using MATLAB's Symbolic Math toolbox, but it is complicated and covers several pages. We have therefore omitted it from the main text (in Appendix C, we provide the code for finding the solution), but the final equation used to generate the CFFs is provided online. To aid discussion we denote the solution as $\Phi(I)$.

We substituted Equations 8 and 9 with $S(f) = 1/I$ into the solution to Equation 7 to give a general formula relating CFF to I, which depends on six constant parameters: G_{max}, I_{50}, a, b, f_{cL}, and k; *i.e.*, the CFF is $\Phi\left(I \middle| G_{\max}, I_{50}, a, b, f_{cL}, k\right)$.

We fitted Φ to the historical CFF data by allowing just G_{max} and I_{50} to vary. The fit was good at medium and high intensity levels, but poor at levels below about 0 $\log_{10}$ photopic Td. Given that the available TCSF data on which the original model was based did not extend below about 0.5 $\log_{10}$ Td, this is unsurprising. There are two obvious reasons for the discrepancies below 0 $\log_{10}$ photopic Td. First, k, the strength of feedforward inhibition was incorrectly assumed to be fixed even at low I. Second, the power law function (Equation 9) incorrectly allows the speed of processing, f_c, to decline indefinitely (or equivalently, the

integration time to increase indefinitely) with decreasing *I*. While these assumptions are consistent with TCSF data above 0.5 $\log_{10}$ Td (Rider et al., 2019), they may not be appropriate at the lower light levels used for some CFF measurements.

Measurements of bipolar and ganglion cell responses suggests that the inhibitory mechanisms in the retina, and thus *k*, become weak or non-existent at very low light levels, even for cone-mediated vision (see Barlow et al., 1957; Chan et al., 1992; Thoreson and Mangel, 2012). To accommodate the extended CFF data at low light levels, we now incorporated this finding into the model by allowing *k* to decline at very low levels according to a sigmoidal function:

$$k = \frac{0.8\,I}{I + I_k}, \qquad (10)$$

where I_k, the light intensity at which *k* is reduced by a half its maximum value of 0.8, was set to $10^{-0.5}$.

Allowing f_c to decline indefinitely with *I* is incompatible with the concept of a lower limit's being set by the dark light or eigengrau (Barlow, 1956, 1972; Gibson and Waddell, 1952). To avoid the unreasonably small values of f_c at low levels, we added a variable term, I_b, into the general formula for the CFF, so that *I* is replaced by $I + I_b$ in Equations 8 and 9. This prevents f_c from becoming too small at low light levels, so approximating the system's hypothetical dark light, but also, as we show below, having the additional effect of allowing us to account for the effect of the real backgrounds on the L- and S-cone CFFs.

The steady background lights in our experiments have relatively little effect on the gain (which is approximately constant at low levels, [see Equation 8], but increase the variable corner frequencies at low levels, [see Equation 9]). The effect of the background on the system is therefore mainly to speed it up at low *I*, causing a steep decline in the CFF with decreasing *I* at the lowest intensities. We fitted $\Phi\left(I + I_b \middle| G_{\max}, I_{50}, a, b, f_{cL}, k\right)$ to the historic CFF data, allowing just three parameters, $\log_{10} G_{max}$, $\log_{10} I_{50}$ and $\log_{10} I_b$, to vary. The best fitting parameters (±standard errors) were 12.26 (±0.008), 3.40 (±0.021) and 0.92 (±0.017), respectively, with RMSE = 0.0257 and adjusted R^2 = 99.1%. The functions relating f_{cL}, f_c, *G* and *k* to *I* for the historical data are shown as the red curves in Panels **B**, **C** and **D** of Figure 5, where they can be compared with the original functions used by Rider et al. (2019).

Although somewhat speculative at low *I*, for the reasons given above, the model fit shown by the leftmost cream-coloured curve in each of Figures 6**A** and 6**B** (in double and single logarithmic coordinates, respectively) is remarkably good. The historical data are shown as light grey symbols and the empirically derived template is shown as the black curve.

[Insert Figure 6 about here]

Fitting the general formula to the L-cone and S-cone CFF templates at low *I* is complicated using steady backgrounds to isolate the L- or S-cone responses at lower cone excitation levels. These backgrounds reduce the contrast of the flicker and do so differently for the three cone types as well as for the post-receptoral pathways that combine different cone signals. But since $S(f)$ in Equation 7 is the amplitude sensitivity, it is only the amplitude and not the contrast of the flicker that is important. The most important effect of the backgrounds is to prevent complete dark adaptation, thus limiting the lowest corner frequencies reached as target radiance is decreased.

Another complication is that the backgrounds and targets are of very different wavelengths both for the L- and for the S-cone measurements, so that at lower temporal frequencies and lower intensities, the flicker detection may be mediated by chromatic pathways (e.g., Estevez and Cavonius, 1975; Stockman et al., 1991). Accordingly, we excluded from the fits data below 6.5 and 6.6 $\log_{10}$ quanta s^{-1} deg^{-2} from the aligned L- and S-cone data, respectively (corresponding to 0.0 and -0.12 $\log_{10}$ Td in Figures 6**A** and 6**B**). For the L-cone data, the 481-nm background causes the L-cone CFF data to fall short of the historical CFF data below about 1 $\log_{10}$ Td (see brown shaded area in Figure 4). This can be accounted for by increasing the background term, I_b. We fitted the model to the original L-cone template shown in Figure 2**A**, allowing for a lateral shift of 6.5 $\log_{10}$ units in the luminance axis, which is consistent with the horizontal shift required to align the L-cone CFF data with the historical data. This shift mainly accounts for the L-cone target intensity's being given in $\log_{10}$ quanta $degree^{-2}$ sec^{-1} whereas the historical data and model are given in trolands, but it also reflects smaller shifts due to the use of different experimental conditions and stimulus parameters. We allowed G_{max}, I_{50} and I_b to vary in fitting the model and obtained best-fitting estimates of $\log_{10} G_{max}$ = 12.29 (±0.024), $\log_{10} I_{50}$ = 2.35 (±0.038) $\log_{10}$ Td and $\log_{10} I_b$ = 1.41 (±0.054) $\log_{10}$ Td, with RMSE = 0.0293 and adjusted R^2 = 97.7%. The fit is shown by the cream curves in each of Figures 6**A** and 6**B** (in double and single logarithmic co-ordinates,

respectively) along with the aligned L cone data from Figure 2**A** (pink symbols) and the empirically derived non-parametric template (dark red curve).

For the S-cone CFFs the data also fall more steeply than the historical CFF data at lower levels, which we assume is due to the steady 620-nm background in our experiments. In this case, unlike the L-cone case, the effect of the background on the S-cones must be indirect, since the S-cones are insensitive to 620-nm light (Stockman et al., 1999). Thus the effect is likely to be due to opponent interactions with the L- and M-cones (for review, see Smithson, 2014). Alternatively, it has been shown that cones and ganglion cells adapt over different light levels in both the magnocellular and parvocellular pathways with the ganglion cells adapting before the cones (Dunn et al., 2007). If the same is true in the koniocellular pathway, which receives significant input from all three cone types, the background will strongly activate the L- and M-cones and cause the ganglion cells in that pathway to light adapt and speed up thereby reducing sensitivity to the weak S-cone signals at lower target levels. In either case, we assume that the interaction can again be accounted for by adding a steady background term, I_b, and we fitted the same model to the S-cone template from Figure 2**A**, again allowing a lateral shift of 6.72 $\log_{10}$ units to account for the different luminance scale here compared to the model. [The shift of 6.72 $\log_{10}$ units is the L-cone shift of 6.50 $\log_{10}$ units adjusted by 0.22 $\log_{10}$ unit to account for the L- and S-cone spectral sensitivity differences and prereceptoral absorption at 440 nm affecting the S-cone measurements (Stockman and Sharpe, 2000).] The best fitting estimates are $\log_{10} G_{max}$ = 11.82 (±0.039), $\log_{10} I_{50}$ = 1.75 (±0.086) $\log_{10}$ Td and $\log_{10} I_b$ = 0.96 (±0.055) $\log_{10}$ Td, with RMSE = 0.0347 and adjusted R^2 = 96.7%. The fit is shown by the cream-coloured curves in each of Figures 6**A** and 6**B** (in double and single logarithmic co-ordinates, respectively) along with the aligned S-cone data (pale blue symbols) from Figure 2**A** and the empirically derived non-parametric templates. Again, the fit is good up to the point where the S-cone data plateau and M-cones begin to have an effect (Stockman and Plummer, 1998).

4.4 Implications of the model

All the data, including the historical and the L- and S- cone measurements can be fit with this same light adaptation model by adjusting just three model parameters, G_{max}, I_{50} and I_b. Moreover, the adjusted parameter values are all plausibly related to the expected quantal

sensitivities of the receptors and pathways. Additionally, over most of the intensity range, only two parameters are needed, since I_b is only needed to account for the effect of backgrounds at very low intensities below about 1 $\log_{10}$ Td. In this section, we consider how the 3 parameters affect the CFF and how the parameters each relate to the Ferry-Porter law.

The effect on the CFF of varying two of the model parameters, I_{50} and I_b, is apparent in Figure 6 in which the historical data are shown by grey symbols and the L- and S-cone data by red and blue symbols, respectively. Increasing I_b, by introducing a background as seen with the L-cone data (I_b = 1.41) compared to the historical data (I_b = 0.92), causes a steeper decline at low levels, consistent with the data, and meaning that higher intensity targets are required to see any flicker in this low-level region. In contrast, I_b has relatively little effect at higher levels since the increasing target intensity means that the contribution of the background to the effective intensity becomes negligible. The effect of varying I_{50} can also be seen in Figures 6**A** and 6**B** where the CFF functions flatten at lower luminance and lower CFF values for the S-cone data ($\log_{10} I_{50}$ = 1.75) compared to the L-cone ($\log_{10} I_{50}$ = 2.35) and historical data ($\log_{10} I_{50}$ = 3.40).

The effect of varying G_{max} (the maximum gain in the dark) on the *log*(CFF) versus *log*(*I*) shape is illustrated in Figure 7 where CFF on a log scale is plotted against log light level for several values of log G_{max}. The solid dark blue curve is the fit to the historical data shown also in Figure 6 and has f_c changing with light level according to Equation 9. The other colours and lines, with the exception of the dashed white curve which we will discuss below, represent successive reductions of $\log_{10} G_{max}$ by 0.3 $\log_{10}$ units from 12.29 to 10.79 $\log_{10}$ units all accompanied by the change in f_c given by Equation 9.

[Insert Figure 7 about here]

The differences in double logarithmic coordinates produced by reductions in $\log_{10} G_{max}$ from 12.29 to 10.79 $\log_{10}$ units primarily cause a diagonal shift of the predicted CFF functions down and to the right. The functions also become progressively more tightly curved, so that the initial steep vertical rise and the horizontal plateau are closer together at lower gains than high; nonetheless, the functions can be approximately aligned by shifting them up and left. Moreover, consistent with much of the clinical CFF data described next in Section 4, the ratio of vertical to horizontal shifts is approximately 1:4. We have adjusted

the aspect ratio of this figure so that such shifts fall along the 45° diagonal, and we return to this feature later.

It seems intuitive that the speeding up of the visual response with increasing mean intensity should allow us to see faster flicker. However, Equation 7 suggests that the speeding up has relatively little effect on sensitivity to frequencies approaching the CFF [as CFF >> f_c, see Rider *et al.* (2019)], and in fact would lead to a slight reduction in CFF. This is because the left-hand side of Equation 7 is 1/*I* at the CFF (and so is independent of both flicker frequency and corner frequency); any increase in f_c on the right-hand side (affecting primarily the first term in the denominator) must be offset by a reduction in *f* to rebalance the equation, and *vice versa*. This counterintuitive finding is clearly demonstrated in Figure 7, in which the dashed white curve shows how the historical CFF fit changes if instead of the corner frequency increasing with increased light level from about 6.39 to 21.07 Hz according to Equation 9 (dark blue line), it remains fixed at 6.39 Hz. The differences between the varying and fixed corner frequencies are small with the CFF slightly (3.7 Hz or 0.03 $\log_{10}$ unit) *lower* at the highest levels even though the corner frequency has increased by 0.50 log unit.

This shows that under bright conditions we can see faster flicker because the amplitude of the flicker itself has been increased (because, for the fixed contrast stimuli used in CFF experiments, the amplitude is always in the same proportion to the mean luminance); our seeing faster flicker with increasing light level is not as a direct consequence of the system becoming faster (see, for example, Rider et al., 2019).

That is not to say, of course, that the speeding up is not important. If the visual system were to remain sluggish at higher light levels, the integration time of the system would be too long and the response to low frequencies and steady lights would rapidly overwhelm the visual system as neurons reach their maximal response. Conversely, if the visual system were to speed up too much in relation to the increase in light level, then overall sensitivity would be reduced to the extent that vision would be significantly impaired. Alternatively, starting from the fast processing at high light levels, the visual system could respond to the same range of frequencies at low light levels if it somehow increases the gain to account for the reduction in light level, the reverse process of MacLeod's "dark glasses" analogy (MacLeod, 1978). However, it is not clear how the visual system could boost the signal in this way, and it would render the system more susceptible to high-frequency noise in low light conditions, so an

alternative mechanism is used by which the visual system slows down to increase temporal integration and restore sensitivity to lower frequencies. Given the constraint of neuronal response ranges, an appropriate change in speed is therefore essential to allow us to see fast flicker without overloading the system, however the increase in speed at higher levels is not directly responsible for our ability to see faster flicker in brighter conditions. Consequently, we suggest that little if any information about the speed, or how it changes with light level, can be derived directly from the CFF alone. To assess how speed changes with light level requires additional measurements at multiple light levels, such as TCSFs (e.g., Rider et al., 2019; Stockman et al., 2021). Our model supports the alternative explanation that the steeper Ferry-Porter slopes imply a higher gain. A corollary of this is that although S-cone pathways are slower than L-cone and luminance pathways (*i.e.*, have longer integration time) (Krauskopf and Mollon, 1971) and S-cone CFFs are lower than L-cone CFFs, these two facts are only indirectly related. The model suggests that the lower S-cone CFFs are primarily due to lower gain ($\log_{10} G_{max}$ = 11.82 for the aligned S-cone CFF data, and 12.26 and 12.29 for the historic and L-cone CFF alignments, respectively).

5. Clinical CFF measurements

We have shown that the shape-invariant templates and model provide plausible descriptions of normal CFF versus *I* data measured under a variety of different conditions. However, the Ferry-Porter slopes of the normal data vary by a factor of less than about 4. A stronger test of the shape-invariant model is to add to the analysis our extensive set of clinical CFF data, some of which show substantial reductions in Ferry-Porter slopes and in overall CFF. We ask if the same shape-invariant templates and the same model predictions illustrated in Figure 7 can also account for the clinical measurements. In performing this analysis, we bring together for the first time CFF measurements made in our laboratory in patients with pathogenetic variants in eleven different genes.

5.1 Patient groups and gene defects

The yellow box in Figure 8 lists the eleven clinical diseases (**A)-(K**) for which we measured CFFs. The affected genes are given in parentheses and their locations are indicated by the

letters A-K inside red circles shown in the simplified schematic representation of the retina on the left of the figure and in the photoreceptor outer segment in the upper right of the figure. We discuss the effects of the individual gene defects in more detail later.

[Insert Figure 8 about here]

Table 2 lists the diseases, the affected genes, the number of patients who carried out the L- and S-cone CFF measurements, the patient codes, and the data sources. More details of the molecular genetics and genetic variants and the effects of the diseases can be found in the original publications (we have used the same patient codes here as in the original publications). The flicker sensitivity measurements for the diseases noted by an asterisk in the leftmost column of Table 2 were modelled and discussed in Stockman, Henning & Rider (2021). The affected genes and patient codes are also given in the keys of Figures 9 and 10 along with the symbols used for each CFF function. The ages of the patients are noted in the legends of Figures 9 or 10. L-cone CFF data are shown for forty patients in Figure 9 and S-cone CFF data are shown for twenty-two patients in Figure 10.

	Disease	Affected gene	Patient numbers for L or S	Patient codes	Sources
(A)	X-linked cone dystrophy	*OPN1LW/ OPN1MW*	2 (L)	IV:1:1, IV:4	Gardner *et al.* (2010)
(B)*	Rod monochromatism	*GNAT2*	2 (L)	Father, Son	Stockman *et al.* (2007b).
(C)*	Autosomal dominant progressive cone dystrophy	*GUCA1A*	4 (L)	GP1 to GP4	Stockman *et al.* (2014b)
(D)	Autosomal dominant progressive cone rod dystrophy	*GUCY2D*	1 (L) 1 (S)	IV:1	Mukherjee *et al.* (2014)
(E)*	Bradyopsia	*RGS9*	1 (L) 1 (S)	-RGS9-1	Stockman *et al.* (2008)
(F)*	Leber's congenital amaurosis 2	*RPE65*	5 (L)	S1, S3, S5, S6, S12	Ripamonti *et al.* (2014b).
(G)	Early onset retinal dystrophy	*LRAT*	3 (L)	P1 to P3	Dev Borman *et al.* (2012)
(H)*	Progressive cone dystrophy	*KCNV2*	5 (L) 3 (S)	SR1 to SR5	Stockman *et al.* (2014a).
(I)*	Enhanced S-cone syndrome	*NR2E3*	4 (L) 6 (S)	ES1 to ES6	Ripamonti *et al.* (2014a)
(J)	Congenital stationery night blindness	*GRM6*	2 (L)	*GRM6*-S1, *GRM6*-S3	Ba-Abbad (2018)
(K)*	Autosomal dominant optic atrophy	*OPA1*	11 (L) 9 (S)	P1 to P11	Majander *et al.* (2017).

Table 2: Summary of clinical data and sources

5.2 Patient CFF data in double-logarithmic co-ordinates

In this section we show that all the patient measurements can be fit by the same double-logarithmic template developed for normal observers with simple horizontal and

vertical shifts; that is, the patient data also conform to the same theoretical framework as those of the normal observers. Figure 9**A** shows a plot of the individual patient L-cone CFF *versus I* data. As might be expected, there is considerable variability among the data sets. Nevertheless, like the normal CFF data plotted on these coordinates, the patient functions all have an approximately similar common shape. Remarkably, the differences among the individual clinical CFF data can also be accounted for by horizontally and vertically shifting a shape invariant template. Furthermore, before shifting, the form of the patient L-cone CFF data in Figure 9**A** is strikingly like the form of the model predictions for changes in G_{max} shown in Figure 7. Figure 9**B** shows the patient CFF functions shifted to align with the L-cone CFF template derived from the normal CFF data shown first in Figure 2. With few exceptions, the individual functions align well with the L-cone template. The horizontal and vertical shifts required to align each data set with the template are plotted in Figure 11**A**. The average mean squared errors of the fits are 0.0013 and 0.0020 $\log_{10}$ Hz for the L-cone and S-cone shifts, respectively.

[Insert Figure 9 about here]

Next, we switch to S-cone patient CFFs. Figure 10**A** shows a double-logarithmic plot of the individual clinical S-cone CFF versus *I* data. The key shows the symbols used for each patient, using the same code as for the L-cone measurements. The key includes new symbols for two additional patients, ES5 and ES6, who only carried out S-cone measurements. Like the L-cone data, the patient S-cone CFF data conform to a common template shape when plotted in these coordinates. Figure 10**B** shows the individual CFF functions shifted to align with the S-cone CFF template derived from the normal CFF data and shown in Figure 2. The horizontal and vertical shifts required to align each data set with the template are again plotted in Figure 11**B**. The individual functions align well with the S-cone template shape, although there are some deviations and outliers.

[Insert Figure 10 about here]

The horizontal and vertical logarithmic shifts required to align the individual patient and normal observer CFF data with the normal templates have been plotted in Figure 11**A** for the L-cone data and in Figure 11**B** for the S-cone data. For the patient data, we have used the same symbols as those in Figures 9 and 10, while for the normal data we have used dark red (L-cone) and blue (S-cone) crosses (see figure key). Relative to the normal template,

positive shifts in $\log_{10}$ CFF (upward shifts) indicate poorer performance compared to the mean normal observer, and negative shifts better performance. Negative shifts in $\log_{10}$ radiance (leftward shifts) indicate poorer performance than normal, and positive shifts better performance.

[Insert Figure 11 about here]

The shifts required to align the normal CFF data with the templates are relatively small and cluster around horizontal and vertical shifts of (0,0). The shifts required for the patient data are much more variable. Pure horizontal shifts are consistent with among other possibilities, changes in the effectiveness of the light, a simple example of which would be a change in quantal sensitivity caused by pre-receptoral opacities. As discussed below, combinations of vertical and horizontal shifts are consistent with gain changes after photon absorption. A pure vertical shift corresponds to a constant multiplicative change in CFF at all light levels, but it is difficult to envisage a biological mechanism that would cause such a shift. Some of the shifts, notably those for four of the patients with the *KCNV2* defect, conform to pure vertical or horizontal shifts. However, for most of the L-cone CFF data, the shifts lie along the diagonal indicated by the dashed line with a slope of -0.26 Hz per $\log_{10}$ unit (-4 to 1 on these coordinates). Thus, along this line, for every vertical $\log_{10}$ unit shift of the CFF data there is a horizontal shift of about 4 $\log_{10}$ units. The potential significance of this is discussed next.

5.3 Implications of the shifts of the clinical data

Figures 9**B** and 10**B** show clearly that the shape-invariant L-cone and S-cone templates provide plausible descriptions of the CFF functions measured in patients with eleven different eye diseases. The differences between patient and normal observer CFF data can be characterised by horizontal and vertical shifts of the data in a double-logarithmic space. But what do these template shifts relate to physiologically, and how do they relate to the model?

Template shifts caused by changes in gain are likely to depend on where in the processing sequence the gain change is introduced. A change in gain at the beginning of the processing sequence (such as caused by a change in lens opacity or putting on dark glasses)

would be expected to cause predominantly horizontal shifts in the CFF function, since the change is equivalent to changing I and I_{50} but not G_{max}. By contrast, a change in gain at the end of the processing sequence is equivalent to changing G_{max} in our model while keeping everything else fixed. As shown in Figure 7, changing G_{max} approximates to vertical to horizontal shifts in the ratio of 1:4. Notably, the optimal shifts of L-cone clinical CFF data shown in Figure 11**A** conform to this ratio, falling along the diagonal indicated by the dashed line with a slope of -0.26. Importantly, the L-cone patient shifts shown in Figure 11**A** suggest the general model is applicable to patients as well as to normal observers.

In many defects, the gain change is likely to be neither early nor late in the processing sequence or may even be introduced at several stages in the sequence, so that the required horizontal and diagonal shifts will conform neither to simple horizontal shifts nor to diagonal shifts in the ratio 1:4.

Alternatively, the finding that the horizontal and vertical shifts of the clinical L-cone CFF data required to align with the normal template frequently fall along a -4:1 diagonal (dashed line, Figure 11**A**) can be related to power-law behaviour discussed in Section 4.3. The finding may suggest that at the much lower CFFs experienced by most patients only four of the six stages in the model have approached the power law region defined by Equations 5 and 6 (so that effectively n=4), while the two remaining stages retain a relatively flat response at frequencies near the CFF (because $f << f_c$). The *log*(CFF) versus *log*(I) function will than have a slope of 1/4 rather than 1/6 and consequently changes in gain will shift the CFF along a 1:4 diagonal—as we find for patients. Although our original model was not developed with patient data in mind (nor for CFF data more generally), we previously found that the best fit to normal TCSF data meant four LP-stages with variable and lower corner frequencies and two LP-stages with fixed but high corner frequencies (Rider et al., 2019). Consistent with this idea the normal L-cone template approximates a 1/4 slope over a lower part of its range but then reaches a slope of 1/6.

5.4 Individual diseases

So far, we have discussed and analysed the clinical CFFs mainly in general terms. In this section, we discuss the clinical CFFs on a disease-by-disease basis, linking the results to the

underlying gene defects. The following text refers to the CFF data plotted in Figures 9 and 10 and to the template shifts plotted in Figure 11. The symbols used for the patients are given in the figure keys of Figures 9, 10 and 11. Following Figure 8, we discuss each of the eleven diseases in the order **(A)** to **(K)**. For semi-logarithmic plots of the patient CFF data and descriptions of the Ferry-Porter slopes, please refer to the original publications.

For seven of the diseases (noted by asterisks in the subsection titles below), we have separately measured and modelled L-cone flicker sensitivity (TCSF) data. Measuring the full TSCF, rather than just the CFF, allows us to estimate processing speed (*i.e.*, f_c). Consequently, for those seven diseases we can infer how each disease changes the speed of processing, and the response gain at one or more light levels. As we previously reported, based on the TCSFs, the patient losses, in general, can be explained by changes of speed or gain associated with one or two low-pass-stages (Stockman et al., 2021). According to the model applied here, the changes in gain should shift the position of the CFF template shape in double-logarithmic coordinates but changes in speed should have little *direct* effect on the shape or position of the template.

In Section 7.3 and figure 14 of Stockman *et al.* (2021), we speculated about how each of the steps in the sequential model shown Figure 5**A** might link to underlying physiology and anatomy (reviewed by Rider et al., 2019). In brief, we postulated that the first three LP-stages [1-3] are in the cones or their pedicles, [4] is later in the retina, and [5] and [6] are after the retina perhaps in the cortex. The feedforward stages, [**A**] and [**B**], with their associated level controls, *k*, and sign inversions are assumed to be in lateral connections mediated perhaps by horizontal cells The gain control, *G*, is placed early where photopigment bleaching attenuates the input signal; however, other gain-control processes (subsumed under *G*) will occur throughout the network. The locations of these steps can be compared with those of the affected genes shown in Figure 8.

(**A**) *X-linked cone dystrophy* Patients IV:1:1 and IV:4 suffered from X-linked cone dystrophy caused by a missense mutation of the L- and M-cone opsin genes (*OPN1LW* or *OPN1MW*), which results in protein misfolding leading to the loss of L- and M-cone function (Gardner et al., 2010). Accordingly, the two patients show severe losses in L-cone CFF in Figures 9**A** but slight improvements in the S-cone CFF in Figure 10**A**. The leftwards and upwards shifts required to align the L-cone CFF for IV:1 with the normal template (plotted in Figure 11**A**)

are significant (no shifts are given for IV:4 since there was only a single CFF point), which is consistent with substantial loss of L- and M-cone function. In contrast, much smaller downwards and either leftwards (IV:1) or rightwards (IV:4) shifts are required to align the S-cone CFFs with the normal template (Figure 11**B**). These modest shifts are on the edge of the normal range but are consistent with a loss of cone-opponent antagonism in the S-cone pathways caused by the loss of L- and M-cones.

(**B***) *Rod monochromatism* Two patients suffered from achromatopsia caused by a defect in *GNAT2*, a gene that encodes the α-subunit of the cone G-protein transducin (see **B** in Figure 8). Without cone α-transducin, patients should be rod monochromats without cone function, and by conventional measurements both patients would be diagnosed as suffering from complete achromatopsia. However, we discovered that a cone CFF could be measured at photopigment bleaching levels (which are rarely used to measure visual performance in rod monochromats) that had a cone spectral sensitivity and survived a rod bleach. We concluded that cone vision is sustained at bleaching levels in remnant cones by a sluggishly produced photobleaching product that secondarily activates the transduction cascade (see Stockman et al., 2021; Stockman et al., 2007b). Both patients, however, show a devasting reduction in L-cone CFF. Their CFF data require large leftwards and upwards shifts to align with the normal template indicative of the low light sensitivity of the secondary activation of the cascade. Like the shifts for IV:4, the shifts for these patients follow the -4:1 shift ratio shown by the dashed line in Figure 11**A**.

(C*) *Autosomal dominant, progressive cone dystrophy* Patients GP1 to GP4 suffered from autosomal dominant, progressive cone dystrophy caused by a missense mutation in the *GUCA1A* gene encodes a guanylate cyclase activating protein (GCAP), a protein that helps to restore cGMP following its light-activated hydrolysis by the activated effector molecule PDE6 (Payne et al., 1998) (see **C** in Figure 8). This defect causes the activation of retinal guanylate cyclase 1 (RetGC1) at lower light levels, which inappropriately speeds up the offset of the visual response by rapidly restoring cGMP. In the youngest patient (GP1), we found a speeding up of the response in the TCSF data, but the progressive nature of the disease led to a marked slowing down of the response in older family members (see Stockman et al., 2014b; Stockman et al., 2021). These changes are reflected in the required L-cone CFF shifts shown in Figure 11**A**. All four patients require leftwards shifts of about 1.5 $\log_{10}$ units but upwards shifts that

vary from 0.0 to about 0.5 $\log_{10}$ units, depending on age. The increasing upwards shifts may be consistent with a progressive loss of photoreceptors. The leftwards shifts suggest that the speeding up of the response has somehow reduced the effectiveness of the light without changing the overall gain.

(D) *Progressive autosomal dominant cone rod dystrophy* Patient IV:1 suffered from progressive autosomal dominant cone rod dystrophy caused by a defect in *GUCY2D*, a gene that encodes RetGC1. The mutation is believed to cause a gain of function that increases the affinity of RetGC1 for GCAP at low light levels, and thus should inappropriately speed up the visual response at those levels (Mukherjee et al., 2014; Wilkie et al., 2000). However, this patient shows substantial losses in both L-cone and S-cone CFFs, which suggests that the effects of progressive damage and photoreceptor degeneration (Kelsell et al., 1998; Perrault et al., 1999b) has limited the CFF and masked any speeding up of the response even though the patient was only 21 years of age. To align with the normal L-cone template, the L-cone CFF must be shifted leftwards by nearly 2.0 $\log_{10}$ units and upwards by 0.6 $\log_{10}$ unit, close to the 4:1 ratio, shown by the dashed line. The S-cone shifts are smaller but are also indictive of damage.

(**E***) *Bradyopsia* Patient -RGS9-1 suffered from bradyopsia caused by a defect in *RGS9-1*, a gene that encodes a GTPase accelerating protein in the transduction cascade (see **E** in Figure 8). This protein increases the rate of deactivation of the α-transducin-PDE6 complex after its activation by light and thus slows down the visual response and causes a disease known as bradyopsia or “slow vision” (Nishiguchi et al., 2004). Despite this, the L-cone CFF in Figure 9**A** rises normally at lower radiances but then asymptotes at about 22 Hz, while the S-cone CFF in Figure 10**A** rises and then asymptotes at about 12 Hz. As inferred from TCSF data, the slowing down of the visual response in this patient is compensated for by the speeding up of other stages, but this compensatory mechanism fails at moderate light levels (Stockman et al., 2021; Stockman et al., 2008), which results in the low asymptotic CFFs. Figure 11 shows that a modest upwards shift is required to align the L-cone CFF with the normal template, while upwards and rightwards shifts are required to align the S-cone CFF. The early asymptotes in both the L-and the S-cone CFF data, however, make the fits to the templates poor.

(**F***) *Leber’s congenital amaurosis 2* Patients S1, S2, S5, S6 and S12 suffered from Leber’s congenital amaurosis 2 caused by mutations in *RPE65* (see **F** in Figure 8), a gene that encodes

a key component in the retinal pigment epithelium based visual cycle, which restores photopigment after it is bleached by light (e.g., Gu et al., 1997; Marlhens et al., 1997; Perrault et al., 1999b; Redmond et al., 1998). Cones but not rods can regenerate photopigment by way of a second cycle involving Mueller cells, thus enabling cone-mediated vision in younger patients, but older patients become blind in the third or fourth decade of life (Hanein et al., 2004; Perrault et al., 1999a; Wang and Kefalov, 2011; Wu et al., 2004; Znoiko et al., 2002). Figure 9**A** shows that all patients have substantially reduced L-cone CFFs indicating that their vision is severely compromised. In Figure 11**A**, the L-cone CFFs for four of the patients required upwards and leftwards shifts in the approximate ratio of -4:1 to align with the normal template, which is consistent with a reduction in gain. The L-cone CFF data for patient S6 requires mainly a vertical shift. The progressive loss for the patients correlates with the leftwards shifts, which may reflect photoreceptor loss and a reduction in the visual effectiveness of lights.

The Ferry-Porter slopes for these patients range from about 2.35 to 5.45 Hz per decade (see Ripamonti et al., 2014b). Yet, despite these differences in slope, TCSF data for the same patients show little evidence for differences in processing speed (Stockman et al., 2021), thus supporting our contention that these differences in CFF reflect mainly gain changes.

(**G**) *Early onset retinal dystrophy* Three patients P1, P2 and P3 suffer from early onset retinal dystrophy caused by a defect in *LRAT* (see **G** in Figure 8), a gene that encodes an enzyme called lecithin retinol acyltransferase found in the retinal pigment epithelium that is part of the visual cycle that restores bleached photopigment (Ruiz et al., 1999). Deficiency of LRAT results in an insufficiency of 11-*cis*-retinal and reduced levels of visual pigment (Senechal et al., 2006) and leads to photoreceptor death (Batten et al., 2004; Fan et al., 2008). The losses of L-cone CFF indicated by the shifts in Figure 11**A** are variable. The CFFs for P1 require a large leftwards shift of more than 3.0 $\log_{10}$ units, whereas those for P2 and P3 require smaller leftwards and upwards shifts that fall along the -4:1 diagonal, consistent with a reduction in gain.

(**H***) *Progressive cone dystrophy* Five patients SR1 to SR5 (three of whom SR1, SR2 and SR4 carried out S-cone measurements) suffered from progressive cone dystrophy caused by pathogenic variants in *KCNV2*, a gene that encodes a voltage-gated potassium-channel-modifying subunit in the rod and cone photoreceptors, a mutation of which may disrupt the

resting potential of the cones leading to a compromised cone output signal (see **H** in Figure 8) (Salah et al., 2008; Thiagalingam et al., 2007; Wissinger et al., 2008; Wu et al., 2006). Except for SR5, the patients show a consistent pattern of L- and S-cone loss in that the CFF data require a leftwards shift of approximately 1.7 $\log_{10}$ units to align with the L-cone template and of about 1.1 $\log_{10}$ unit to align with the S-cone template with little or no vertical shift. Thus, for both types of cone the losses are consistent with a loss of the effectiveness of the light (comparable to a reduction in lens opacity or putting on dark glasses) rather than a change in gain. This may reflect the change in resting potential limiting the size of the visual response without changing the mean response.

The Ferry-Porter slopes for the *KCNV2* patients are fairly similar to each other and to normal observer slopes (see Stockman et al., 2014a). TCSF measurements show that although SR2 and SR4 suffer from significant speed reductions compared to the other patients (Stockman et al., 2021), these have not affected their Ferry-Porter slopes, which again is consistent with our argument that these slopes do not reflect processing speed,

(**I***) *Enhanced S-cone syndrome* Six patients ES1 to ES6 (ES1 to ES4 carried out only L-cone measurements) suffered from enhanced S-cone syndrome caused by a pathogenic variant in *NR2E3*, a gene that encodes for a photoreceptor-specific nuclear receptor (transcription factor) necessary for photoreceptor development. The defect leads to an overpopulation of the retina with S-cones with fewer L-cones and M-cones and a near absence of rods (e.g., Greenstein et al., 1996; Haider et al., 2000; Hood et al., 1995; Jacobson et al., 1990; Kellner et al., 1993; Marmor et al., 1990; Milam et al., 2002; Sharon et al., 2003). Accordingly, ES1 to ES4 have lower L-cone CFFs than normal in Figure 9**A** with losses of up to 4 to 10 Hz, while all six patients show some improvements in S-cone CFF in Figure 10**A**. In Figure 11**A** the L-cone CFF shifts required to align with the normal L-cone template are upwards and leftwards, consistent with a small reduction in gain, whereas in Figure 11**B** the S-cone CFF shifts required to align with the normal S-cone template are downwards and rightwards, consistent with a small increase gain.

(**J**) *Congenital stationery night blindness* Two patients *GRM6*-S1 and *GRM6*-S3 suffered from congenital stationery night blindness caused by a defect in *GRM6,* a gene that encodes metabotropic glutamate receptor 6 (mGluR6), a G-protein coupled receptor in rod and cone ON bipolar cells (Nakajima et al., 1993). Since rod bipolars are exclusively of the ON type, this

defect blocks the transmission of the primary rod signals to the brain and causes complete congenital stationary night blindness (CSNB) (see **J** in Figure 8) (Ba-Abbad, 2018; Dryja et al., 2005; O'Connor et al., 2006; Sergouniotis et al., 2012; Zeitz et al., 2007). With only OFF cone-bipolars, both patients show a moderate reduction in the L-cone CFF compared to normal observers. As shown in Figure 11**A**, the CFF data for *GRM6*-S3 require an upwards shift to align with the normal template, while those for *GRM6*-S1 require the now familiar -4:1 diagonal shift consistent with a significant reduction in gain.

(**K***) *Autosomal dominant optic atrophy* Eleven patients P1 to P11 (nine of whom made S-cone CFF measurements) suffered from autosomal dominant optic atrophy (DOA) caused by a heterozygous mutations in the *OPA1* gene, a gene that encodes an inner mitochondrial membrane protein (Alexander et al., 2000; Burte et al., 2015; Delettre et al., 2000). This disease affects retinal ganglion cells with no evidence of functional or structural abnormalities in the preceding neural stages in the outer retina (Cohn et al., 2008; Johnston et al., 1979; Kjer, 1959; Kjer et al., 1983; Votruba et al., 1998; Yagasaki et al., 1986; Yu-Wai-Man et al., 2010); consequently, the visual losses should be consistent with normal processing before the ganglion cells (see **K** in Figure 8). Most patients show losses for both L- and S-cone CFFs that vary in severity. In Figure 11 the L-cone and S-cone CFF data require mainly upwards and leftwards shifts to align with the normal template, consistent with the disease causing a reduction in gain due to ganglion cell loss.

A review of the molecular basis of these and many other retinal diseases can be found in Berger, Kloeckener-Gruissem & Neidhardt (2010). Details of the phototransduction cascade can be found in several review articles (Arshavsky et al., 2002; Burns and Baylor, 2001; Fain et al., 2001; Perlman and Normann, 1998; Pugh and Lamb, 2000; Pugh et al., 1999).

6. Conclusions and future directions

We have re-examined over one hundred years of CFF data from various laboratories and over twenty years of clinical and control CFFs from Stockman's laboratory at the UCL Institute of Ophthalmology and have shown that they conform closely to a common template when plotted in double-logarithmic co-ordinates, requiring only vertical and horizontal shifts to align all the data. Moreover, the template shape and the shifts can be

accounted for by a relatively simple model of light adaptation and changes in just three parameters of the model, G_{max}, I_{50} and I_b.

The fit of the model to the historical CFF data is extremely good over the full six decades of intensity. The quality of the fits to the S-cone data and particularly to the L-cone data is slightly less impressive, but this is unsurprising given that the model was originally derived to explain data from sources that typically used flickering white lights and thus the same contrasts for all three cone types. As discussed above, to favour flicker detection by either the L- or the S-cones our stimuli contain strong chromatic contrasts between the target and background particularly at low target intensities where detection may then be mediated by chromatic as well as by achromatic pathways (Estevez and Cavonius, 1975; Stockman et al., 1991). Furthermore, both sets of CFF data may be influenced at higher light levels by contributions from M-cones. Indeed, the S-cone CFFs are usually mediated by M-cones at the highest 440-nm target levels simply because the S-cones saturate and the M-cones consequently become more sensitive (Stockman and Plummer, 1998). Although perhaps less obvious, the M-cones may also affect the nominally L-cone CFF measurements at high 650-nm target radiances. Despite the M-cones being over 10 times less sensitive to the 650-nm target and 60% more sensitive to the 481-nm background than the L-cones (Stockman and Sharpe, 2000), the L-cone and M-cone sensitivities to the nominally L-cone CFF target will converge towards higher intensities (see Figure 1 of Stockman and Mollon, 1986). Such a change from predominantly L-cones at low levels to a mix of L- and M-cones at higher levels might explain the discrepancy between our single channel model and the L-cone CFF data, where the fit seen in Figure 6 is too steep at about 1.5-2 log Td, but too shallow at about 2.5-3 log Td.

The common template shape predicted by our model conforms to a logarithmic function in double-logarithmic co-ordinates, thus providing a simple explanation of the long-known but hitherto unexplained Ferry-Porter law. Changes in gain produce changes in the position of the logarithmic function and thus changes in the Ferry-Porter slope. Changes in processing speed on their own do not cause changes in the Ferry-Porter slope.

If our modelling is correct, CFF measurements are somewhat limited in their value as a clinical investigation tool because while the CFFs give a good indication of the overall gain of the visual system they give little indication of its processing speed. Thus, perhaps somewhat

counterintuitively, a lower CFF found in a patient does not necessarily imply that their visual processing is slower than normal. As discussed above, a lower CFF might be indirectly due to a reduction in processing speed as it would prompt a change in gain to prevent low-frequency signals overwhelming the visual system, such as in Leber's congenital amaurosis (*RPE65*) (see Figure 9 of Stockman et al., 2021), or it could be a more direct change in gain caused, for example, by the loss of ganglion cells in autosomal dominant optic atrophy (*OPA1*), the progressive loss of cone function in X-linked cone dystrophy (*OPN1*), or changes in L/M to S cone ratio in enhanced S-cone syndrome (*NR2E3*) that show evidence of reduced gain for L-cone CFF but increased gain for S-cone CFF (see Figure 11). To confirm a change in processing speed requires other measurements in addition to the CFF. It is worth noting that flash detection measurements made as a function of background intensity (e.g., threshold-versus-intensity functions) suffer from a similar confounding of speed and gain with higher sensitivity being associated with either a higher gain or a longer integration time (see Rider et al., 2019). Flicker sensitivity measurements (TCSFs) are particularly useful in this context because they depend on both gain and speed (Stockman et al., 2021). TCSFs, however, depend on flicker sensitivity measurements made as a function of frequency at a fixed *I*, so that to obtain information about the dependence of gain and processing speed on *I*, the measurements must be repeated at several intensity levels. This is laborious and time consuming and although we were able to perform such measurements thanks to the generosity of many patients (summarised in Stockman et al., 2021), it is not an appropriate technique for general use in the clinic.

An alternative approach would be the development of a hybrid CFF test in which CFF is measured at several light levels at two or more contrasts (say 25, 50 and 100% contrast, depending on a patient's flicker sensitivity). The results of such measurements can then be used to evaluate part of the TCSF by determining the slope of the sensitivity loss at high frequencies at each light level (by plotting log contrast as a function of linear CFF) to thus give the "frequency constant" from which the speed of the visual response can be estimated (for details see Stockman et al., 2021), while the gain can be estimated from the 0 Hz intercept. Measuring CFF at different contrasts to estimate the TCSF has been done before (e.g., Conner, 1982). This hybrid method would allow for a relatively simple but thorough investigation of the consequences of any given clinical defect in terms of temporal response and light

adaptation and would be particularly useful for monitoring changes in gain and speed over time or in response to treatments. It could also provide extremely useful information for visual deficits of unknown aetiology, as different patterns of speed and gain changes across light levels will be consistent with deficits in different parts of the visual pathway.

Acknowledgements

The work described has been supported by grants from Fight for Sight, BBSRC, Moorfields Eye Hospital Special Trustees, and the National Institute for Health Research Biomedical Research Centre at Moorfields Eye Hospital NHS Foundation Trust and UCL Institute of Ophthalmology. The current funding is from the BBSRC. We are especially grateful to the patients who willingly gave up so much time to participate in these studies, and without whom this work would not have been possible. We acknowledge the many colleagues and collaborators who contributed to this work and are co-authors in the original studies, but especially Rola Ba-Abbad, Arundhati Dev Borman, Jocelyn Cammack, Caterina João, Vy Luong, Anna Majander, Michel Michaelides, Tony Moore, Caterina Ripamonti, Lindsay Sharpe, Hannah Smithson, and Andrew Webster. We thank Rhea Eskew for helpful comments and suggestions.

Appendices

A. Methodological details

A1. Experimental system

The type of optical system used for our experiments is known as a “Maxwellian-view” system (see Westheimer, 1966) that projects discs of light directly onto the retina (see Figure A1 of Stockman et al., 2021). The two discs in these experiments were a target disc of 4° in visual diameter illuminated by either red 650-nm light or a violet 440-nm light, which was optically superimposed on a second, background disc of 9° in visual diameter illuminated by either a blue 481-nm light or an orange 620-nm light. The observer’s view is thus either of a blue circular disc with a red disc in its centre, or of an orange circular disc with a violet disc in its centre. The main advantage of a Maxwellian-view system is that it

can produce high-intensity, uniform images directly on the retina. Calibration is also straightforward since it involves measuring the light entering the pupil and knowing the retinal area over which the light falls. We use the intensity units of quanta per second per degree squared (quanta s^{-1} deg^{-2}). So, for example, for a 650-nm target light of 9.0 log_{10} quanta s^{-1} deg^{-2} and 4-deg in visual diameter (i.e., filling 12.57 deg^2 of area on the retina), the number of quanta entering the pupil is 12,570,000,000 per second. We used a Xenon-arc lamp as our light source, but LEDs could be used instead to carry out the experiments described here with the intensity of a red or violet LED being temporally modulated under electronic or computer control. One caveat is that the images of the light sources on the pupil must fall within the smallest natural pupil to avoid the intensity being reduced by pupillary constriction at higher light levels.

The combination of a 650-nm target and a 481-nm background favours flicker detection by the long-wavelength-sensitive L-cones, which are more sensitive than the middle-wavelength-sensitive M-cones to the 650-nm light and less sensitive to the 481-nm background (Stockman and Sharpe, 2000). The combination of a 440-nm target and a 620-nm background favours flicker detection by the short-wavelength-sensitive S-cones, which are more sensitive than the L-cones or the middle-wavelength-sensitive M-cones to the 440-nm light and virtually insensitive to the 620-nm background (Stockman and Sharpe, 2000). The combinations also make rod involvement in flicker detection unlikely. Restricting flicker detection to largely either L- or S-cones potentially simplifies the interpretation of the results.

In our experiments, the intensities of the lights were controlled by inserting fixed and variable filters that attenuate the light. Additionally, a fast ferro-electric liquid crystal shutter under computer control was used to vary the intensity of the target light at various temporal frequencies while keeping the time-averaged intensity constant. The form of the flicker was sinusoidal and the amplitude of the flicker was kept at 92% of the mean intensity thus maintaining a fixed contrast of 92%. In the L-cone conditions the blue, 481-nm background was fixed at about 8.20 log_{10} quanta s^{-1} deg^{-2} (which is 2.46 log_{10} scotopic trolands or 1.31 log_{10} photopic trolands). In the S-cone conditions the orange, 620-nm background was fixed at about 11.51 log_{10} quanta s^{-1} deg^{-2} (which is 2.38 log_{10} scotopic trolands or 4.37 log_{10}

photopic trolands). The backgrounds were present in all our experiments except one control experiment using the 650-nm target where they were omitted.

A2. Procedures

All observers light adapted to the background and target for 3 minutes before any measurements were made. The method of adjustment was used to determine threshold, *i.e.*, the observers adjusted the flicker frequency to find the frequency at which the flicker was just visible. The target was flickered sinusoidally at the highest available amplitude on our system (which was 92% of the maximum target intensity) and the time-average radiance set by the insertion of neutral-density filters into the target channel to values ranging from about 6.5 to 11.0 $\log_{10}$ quanta s^{-1} deg^{-2} for 650 nm L-cone target and about 6.5 to 10.5 $\log_{10}$ quanta s^{-1} deg^{-2} for the 440 nm S-cone target. At each target radiance, the observer adjusted the rate of flicker up or down to find the flicker frequency at which the flicker was just visible.

For all measurements, three settings were made and averaged. The process was repeated on each of three separate sessions, usually on separate days, for the normal observers and, on one, two or three separate sessions for the patients depending on availability and time constraints. The mean of the results for each experimental run of three settings was averaged and the standard error across the separate sessions determined. The standard errors shown in the data plots show the variability across sessions for each observer (a lack of error bars means only one session was run).

A3. Calibration

The intensities of the target and background lights were measured at the exit pupil of the optical system using an UDT radiometer, calibrated by the manufacturer (Gamma Scientific, San Diego, CA, USA) against a standard traceable to the US National Bureau of Standards. A spectroradiometer (EG&G, San Diego, CA, USA) was used to measure spectral power distributions of all lights. Full methodological details can be found elsewhere (Stockman et al., 2007a; Stockman et al., 2007b; Stockman et al., 2008).

A4. Data alignment

In a "leave-one-out" procedure, each of the individual CFFs was used in turn as the starting function against which all the other individual CFFs were aligned by horizontal and vertical shifts on the double logarithmic coordinates using a least squares procedure implemented in MatLab. The alignments to the starting function that gave the lowest mean squared error are shown in the figures (with the CFF and *I* values adjusted to the mean values across observers). The same procedure was used for the S-cone CFFs, but the S-cone alignments ignored data above 9.2 $\log_{10}$ quanta s^{-1} deg^{-2} where the CFF is affected both by cone-opponent saturation (Mollon and Polden, 1977) and by the intrusion of other (mostly M-) cones (Stockman and Plummer, 1998)].

B. Normative CFF data

Table B1 gives the normative means and standard errors for the data shown in Figures 2.

Table B1

Mean L-cone CFF data for 21 normal observers plotted in Figure 1A. Column 1 gives the mean radiance of the 650-nm flickering target in $\log_{10}$ quanta s^{-1} deg^{-2}. Columns 2 and 3 give the mean L-cone CFF and two standard errors of the mean, respectively, both in hertz.

Mean target radiance	CFF (Hz)	2 S.E.
6.51	7.00	2.58
6.78	11.32	1.14
7.08	15.06	0.96
7.35	18.23	1.20
7.68	21.11	1.26
7.95	23.19	1.23

8.32	26.46	1.28
8.59	28.76	1.34
8.92	31.95	1.34
9.19	34.48	1.31
9.64	37.34	1.35
9.91	38.54	1.42
10.28	40.25	2.04

Table B2 gives the normative means and standard errors for the data shown in Figures 3.

Table B2

Mean S-cone CFF data for 12 normal observers shown in Figure 1B. Column 1 gives the mean radiance of the 440-nm flickering target in $\log_{10}$ quanta s^{-1} deg^{-2}. Columns 2 and 3 give the mean S-cone CFF and two standard errors of the mean, respectively, both in hertz.

Mean target radiance	CFF (Hz)	2 S.E.
6.54	4.20	0.64
6.83	6.65	0.75
7.13	9.39	0.73
7.42	11.65	0.77
7.74	13.82	0.85
8.03	16.13	0.86
8.39	18.75	0.97
8.70	20.53	0.89
9.02	21.93	1.06
9.31	22.59	1.11
9.61	22.43	1.28
9.90	22.12	1.34
10.26	25.45	1.84
10.57	27.67	2.48

Table B3

Historical, L-cone and S-cone template functions

log *I* (Td)	CFF (Hz)		
	Historical	L-cone	S-cone
-0.85	4.03	--	--
-0.80	4.25	--	--
-0.75	4.47	--	--
-0.70	4.70	--	--
-0.65	4.95	--	--
-0.60	5.21	--	--
-0.55	5.48	--	--
-0.50	5.77	--	--
-0.45	6.07	--	--
-0.40	6.38	--	--
-0.35	6.72	--	--
-0.30	7.07	--	--
-0.25	7.43	--	--
-0.20	7.82	--	--
-0.15	8.22	--	--
-0.10	8.65	--	--
-0.05	9.09	--	--
0.00	9.55	--	--
0.05	10.02	--	--
0.10	10.51	--	--
0.15	10.99	--	--
0.20	11.49	--	--
0.25	12.02	--	--
0.30	12.54	--	--
0.35	13.07	--	5.31
0.40	13.59	--	5.91
0.45	14.10	--	6.58
0.50	14.64	--	7.32
0.55	15.15	8.12	8.13
0.60	15.67	8.96	9.02
0.65	16.21	9.88	9.99
0.70	16.73	10.88	11.07
0.75	17.24	11.97	12.26
0.80	17.76	13.12	13.48
0.85	18.28	14.31	14.78
0.90	18.81	15.52	15.89
0.95	19.33	16.70	16.84
1.00	19.86	17.67	17.65

1.05	20.40	18.61	18.48
1.10	20.97	19.44	19.24
1.15	21.57	20.39	20.06
1.20	22.18	21.35	20.81
1.25	22.79	22.30	21.55
1.30	23.38	23.20	22.27
1.35	23.94	24.03	23.01
1.40	24.49	24.81	23.72
1.45	25.05	25.59	24.47
1.50	25.64	26.36	25.25
1.55	26.27	27.11	26.07
1.60	26.94	27.87	26.90
1.65	27.63	28.61	27.74
1.70	28.31	29.30	28.58
1.75	28.98	29.94	29.40
1.80	29.61	30.63	30.19
1.85	30.26	31.29	30.96
1.90	30.90	31.94	31.71
1.95	31.61	32.58	32.49
2.00	32.32	33.13	33.21
2.05	33.03	33.65	33.95
2.10	33.71	34.17	34.65
2.15	34.39	34.71	35.38
2.20	35.06	35.31	36.14
2.25	35.75	35.96	36.91
2.30	36.44	36.60	37.65
2.35	37.16	37.25	38.42
2.40	37.87	37.90	39.11
2.45	38.58	38.57	39.73
2.50	39.27	39.26	40.34
2.55	39.94	39.91	41.01
2.60	40.58	40.51	41.66
2.65	41.20	41.10	42.16
2.70	41.84	41.71	42.64
2.75	42.49	42.33	43.05
2.80	43.14	42.95	43.42
2.85	43.80	43.54	43.79
2.90	44.43	44.16	44.17
2.95	45.06	44.81	44.57
3.00	45.66	45.54	44.90
3.05	46.26	46.31	45.16
3.10	46.86	47.09	45.45
3.15	47.48	47.83	45.58
3.20	48.11	48.56	45.70
3.25	48.75	49.28	45.82
3.30	49.39	50.02	45.91
3.35	50.03	50.77	45.96

3.40	50.66	51.51	46.01
3.45	51.27	52.20	46.01
3.50	51.89	52.85	46.02
3.55	52.49	53.37	46.04
3.60	52.96	53.82	46.10
3.65	53.42	54.26	46.28
3.70	53.88	54.75	46.44
3.75	54.38	55.17	46.65
3.80	54.88	55.51	46.93
3.85	55.33	55.76	47.24
3.90	55.72	56.03	47.69
3.95	56.08	56.34	48.29
4.00	56.41	56.66	48.77
4.05	56.74	56.95	49.38
4.10	57.06	57.22	50.09
4.15	57.35	57.44	50.86
4.20	57.60	57.66	51.68
4.25	57.84	57.87	52.56
4.30	58.02	58.06	53.42
4.35	58.16	58.25	54.21
4.40	58.33	58.31	54.90
4.45	58.49	58.33	55.55
4.50	58.62	58.34	56.20
4.55	58.74	58.36	56.85
4.60	58.85	58.30	57.52
4.65	58.96	58.24	58.20
4.70	59.06	58.11	58.89
4.75	59.17	57.98	59.57
4.80	59.27	57.85	60.27
4.85	59.37	57.74	60.97
4.90	59.47	57.63	--
4.95	59.57	57.51	--
5.00	59.67	57.39	--
5.05	59.77	57.27	--
5.10	59.87	57.15	--
5.15	59.97	57.03	--
5.20	60.06	56.90	--
5.25	--	56.78	--
5.30	--	56.66	--

C. Model details

C1. MATLAB code for solving Equation 3

Setting $S\left(\hat{f}\right)=1/I$ in Equation 7, where $\hat{f}$ is the CFF and *I* is the amplitude of the flicker, and rearranging, we get,

$$\left(\hat{f}^2+f_c^{\,2}\right)^3\left(\hat{f}^2+f_{cL}^{\,2}\right)-(2\pi)^{-6}GI\left(\hat{f}^2+\left((1-k)f_c\right)^2\right)=0$$

$$F^4+\alpha F^3+\beta F^2+\gamma F+\delta=0,$$

$$\text{where } F=\hat{f}^2$$

$$\alpha=3f_c^{\,2}+f_{cL}^{\,2} \qquad \text{(A1)}$$

$$\beta=3f_c^{\,2}f_{cL}^{\,2}+3f_c^{\,2}$$

$$\gamma=3f_c^{\,4}f_{cL}^{\,2}+3f_c^{\,2}-(2\pi)^{-6}GI$$

$$\text{and } \delta=f_c^{\,6}f_{cL}^{\,2}-(2\pi)^{-6}GI(1-k)^2f_c^{\,2}.$$

Equation (A1) is a quartic in *F* and can be solved explicitly to give four solutions, some or all of which may be complex under a particular set of parameter values, and then the positive square root of any real and positive solutions can be taken to give $\hat{f}$, the CFF. Note that the filter implied by Equation 7 of the main text is a bandpass filter. Thus, under some conditions as well as the high-frequency upper CFF, which is the focus of this paper, there may also be a low-frequency lower CFF below which flicker is not visible. The full set of solutions to Equation A1 is extremely convoluted and is omitted here, but can be found quite simply using Equation A1 and Matlab's Symbolic Math Toolbox:

```
syms F G I fc fcL k
assume(F>0 & G>0 & I>0 & fc>0 & fcL>0 & k>0)
solX = solve(I*G/sym(2*pi)^6 == (F+fc^2)^3*(F+fcL^2)/(F+(1-
k)^2*fc^2), F, 'MaxDegree', 4)
```

Once these solutions are found, we substitute the gain, corner frequency and inhibition strength functions for *G*, f_c, and *k* from Equations 8, 9 and 10 respectively, and solve to get F and its positive square root gives $\hat{f}$ as a function of *I*.

C2. Model adjustments

Equation 9 is a modified version of the original equation given in Rider *et al.* (2019), which was $f_c(I)=\min\left(aI^b,c\right)$, where *a*, *b* and *c* are constants, and min() denotes the smaller

value of its two arguments, aI^b and c. The modification was introduced here in part to simplify the modelling (one fewer parameter) but also because here we found that as G_{max} is reduced in the L-cone or S-cone fits, the speeding up near c was too great relative to the gain reduction, causing a discontinuity in the slope of the CFF. As this discontinuity is not present in the measured functions, we assume it to be an artefact of the modelling and fitted instead the soft-limiting power function, Equation 9, to the f_c parameters from Rider *et al.* (2019). The precise choice of sigmoidal function (we tried many) does not materially affect our results.

Note that in Rider *et al.* (2019), the constant factor of $(2\pi)^6$ in Equation 7 was subsumed into the gain term, denoted by g in Equation 2 of that paper. Accordingly, for direct comparison with the G_{max} values reported here, $6\log_{10}(2\pi) = 4.79$ should be added to the values in the original paper.

FIGURE LEGENDS

Figure 1.

Critical flicker frequencies (CFFs) from observers with normal vision. In panel (**A)**, the symbols show L-cone CFF (Hz) for 21 individual observers as a function of mean log target radiance (log_{10} quanta s^{-1} deg^{-2}) and the assignment of symbols to observers is given in the figure key. Black symbols show the mean CFF and their white error bars are ± 2 standard errors of the mean (S.E.M.) across observers. The means were calculated by interpolation of the individual data where necessary. The solid black line shows the extent of the data consistent with the linear relation between CFF and the logarithm of intensity (the Ferry-Porter law). The data from each observer are averaged from three or more separate runs of three settings each and the error bars are one standard error of the mean (±SEM) calculated between runs. Symbols with fine black outlines indicate observers who carried out both the L-cone and the S-cone measurements. Panel **(B)** shows S-cone data for 12 individual observers again as a function of mean target radiance (log_{10} quanta s^{-1} deg^{-2}). (Note that the abscissa of **(A)** and **(B)** refer to intensities of two different wavelengths.) Black symbols show the mean CFFs and their white error bars are ± 2 standard errors of the mean (S.E.M.) across observers. Again, the means were calculated by interpolation of the individual data where necessary. The solid black line shows the extent of the data consistent with the Ferry-Porter law. Panel **(C):** Illustration of the technique for measuring CFF. The observer varies the frequency of a sinusoidally-flickering light (low frequency at the bottom, high frequency at the top in the illustration) to find the highest frequency at which flicker can just be seen. The mean intensity (horizontal dashed line) and the amplitude of the flicker are kept constant. The CFF data are individual data published previously as mean normal observer data in several publications (e.g., Gardner et al., 2010; Ripamonti et al., 2014a; Ripamonti et al., 2014b; Stockman et al., 2014a; Stockman et al., 2007b; Stockman et al., 2008) using the methods also described in Section 2.

Figure 2.

Aligned CFF data. The CFFs from Figure 1 and using the same symbols, are replotted on a logarithmic axis as a function of log radiance. **(A):** L-cone and S-cone CFFs separately aligned by vertical and horizontal shifts in the double-logarithmic graph. The templates

shown by the solid white (L-cone) and black (S-cone) lines have been separately extracted from the aligned data by LOESS smoothing (see text). **(B):** Alignment of the L- and S-cone data from all the observers with normal vision with the S-cone CFFs shifted according to the alignment, as shown in this panel, of the S-cone template to the L-cone template.

Figure 3.

Historical CFF data. **(A):** CFFs are plotted as a function of log luminance (i.e., on semi-log axes) and the data are taken from eight papers: Porter, 1902 (black stars); Ives, 1912 (coloured hexagons); Hecht & Verrijp, 1933 (white and grey diamonds); Hecht & Shlaer, 1936 (coloured triangles); de Lange 1958 (black and white circles), Giorgi 1963 (coloured half-filled circles); Pokorny & Smith, 1972 (coloured diamonds); and Hamer & Tyler, 1958 (red and green squares). Note, the abscissa is an approximate scale since the luminance units were not always consistent or explicitly stated and because the CFFs have been aligned between 20 and 25 Hz by shifting them horizontally (see text). **(B)*:*** CFFs from **(A)** replotted on a logarithmic axis as a function of log luminance (i.e., on double logarithmic axes). The CFF functions have been aligned by vertical and horizontal shifts in the double-logarithmic graph. In **(B)**, data points from **(A)** that were likely to have been rod mediated were removed. The template (solid white line) was extracted by LOESS smoothing.

Figure 4.

Normal data aligned. CFFs and templates plotted on double logarithmic axes with CFF as a function of log luminance L-cone (white line), S-cone (black line) and historical (dashed black-white line) templates horizontally and vertically aligned over their overlapping regions [about 1.2 and 3.0 $\log_{10}$ Td for all three templates, between 0.5 and 3.0 $\log_{10}$ Td for the L- and S-cone templates and between 1.2 and 4.5 $\log_{10}$ Td between the historical and L-cone templates.]. Individual data are for L-cone (pink symbols), S-cone (violet symbols) and historical CFF data (grey symbols). The cyan symbols show the results of control experiments in which five observers made CFF measurements using our standard 650-nm target but without the 481-nm background used in our other L-cone measurements. The brown shaded area therefore highlights the effect of the steady backgrounds on the L-cone

and S-cone CFFs. The pale green shaded area between luminances 3 and 4.5 highlights the region where the S-cone template deviates from the historical and the L-cone templates.

Figure 5.

Model and model parameters. **(A):** Schematic of light adaptation model from Rider *et al.* (2019). The model components include a gain control (*G*), *6* low-pass (LP) stages ([1]-[6]), and 2 inhibitory feed-forward stages, each of which is made up of a separate LP-stage ([A] and [B]), a gain control (*k*) and a signal inversion (-). The order of these components is not constrained in the model, so that the ordering in the schematic is essentially arbitrary. The smooth curves shown in **(B)** to **(D)** in red are for the fit to the historic CFF data; the original model fits replotted from Rider et al. (2019) are shown as dashed black curves. **(B):** The corner frequency, f_c, of the six variable stages ([1]-[4], [A] and [B]), and f_{cL}, of the two fixed filters ([5] and [6]) both in Hz as functions of mean intensity (I, $\log_{10}$ photopic Tds). The red curve is given by Equation 9 with the background term I_b (see main text) while the dashed black curve is given in Appendix C. **(C):** The gain, *G*, as a function of mean intensity. Both curves are given by Equation 8 with different parameters, see main text. **(D):** The strength of inhibition, *k*, as a function of mean intensity. The red curve is given by Equation 10. The dashed line is the original fixed value of *k* from Rider *et al.* (2019). [Note that the dashed black curves in **(B)** to **(D)** were derived from TCSF data and do not extend below 0.4 $\log_{10}$ Td.]

Figure 6.

Model fits and templates. **(A):** Double logarithmic plots of the model fits (cream lines) to the historic data (grey dots), L-cone data (pink dots) and S-cone data (blue dots). The historical (black line), L-cone (red line) and S-cone (blue line) templates are also shown. **(B):** As in **(A)** but on semi-logarithmic coordinates.

Figure 7.

The effect of changing the gain in the dark, G_{max}, while keeping other parameters constant. (**A**): The dark blue curve is the fit to the historical data from Figure 5, and the

other colours represent successive reductions of 0.3 $\log_{10}$ unit in gain, G_{max}. The dashed white curve shows the model fit to the historical data but with the light-adaptive increase in speed removed. Note the removal of the light-dependant speed change has very little effect on the fit and that the white dashed curve exceeds the "faster" blue curve at higher levels. **(B):** As in **(A)** but on semi-logarithmic coordinates.

Figure 8.

Simplified diagrams of the retinal locations affected by known gene defects in the eleven eye diseases for which we have CFF data. The diseases labelled **(A-K),** and the eleven associated gene defects are listed in the yellow box. Five of the defects are in molecules in the transduction cascade within the photoreceptor outer segment (upper right-hand diagram): Defects in **(A)** *OPN1LW* or *OPN1MW*, which encodes the L- or M-cone opsin; **(B)** *GNAT2*, which encodes cone α-transducin, **(C)** *GUCA1A*, which encodes the guanylate cyclase activating protein (GCAP); **(D)** *GUCY2D*, which encodes guanylate cyclase (GC); and **(E)** *RGS9-1*, which encodes a GTPase accelerating protein (RGS9). Six defects lie beyond the outersegment (left diagram): Defects in **(F)** *RPE65*, which encodes a retinal pigment epithelium-isomerase; **(G)** *LRAT*, which encodes an enzyme called lecithin retinol; **(H)** *KCNV2*, which encodes a voltage-gated potassium channel; **(I)** *NR3E2*, which encodes a photoreceptor-specific nuclear receptor; **(J)** *GRM6*, which encodes a G-protein coupled receptor; and **(K)** *OPA1*, which encodes an inner mitochondrial membrane protein. For more details and the roles of these molecules, see text.

Figure 9.

L-cone patient data. **(A)** CFFs on a logarithmic axis as a function of log target radiance. The white curve shows the mean normal L-cone template. As listed in the figure key on the right, different symbol shapes and colour combinations denote different gene defects, while different patterns within those shapes denote different patients. Orange red triangles denote *GNAT2*, a father (aged 48) and son (24); cyan stars denote *RGS9*, -RGS9-1 (aged 62); black and white hourglass circles denote *GRM6*, blindness *GRM6*-S1 (aged 66) and *GRM6*-S3

(10); red circles denote *GUCA1A*, GP1 (39), GP2 (41), GP3 (51) and GP4 (55); dark grey squares denote *GUCY2D*, IV:1 (aged 21); green diamonds denote *RPE65*, S1 (24), S3 (18), S5 (23), S6 (17) and S12 (19); cyan circles denote *KCNV2*, SR1 (54), SR2 (35), SR3 (29), SR4 (48) and SR5 (44); lime-green squares denote *OPA1*, P1 (aged 13) , P2 (24), P3 (27), P4 (29), P5 (39), P6 (47), P7 (47), P8 (47), P9 (52), P10 (54) and P11 (25); blue hexagons denote *NR2E3*, ES1 (37), ES2 (29), ES3 (39) and ES4 (32); black and white diagonal half-filled squares denote *OPN1LW/OPN1MW*, IV:1:1 (aged 27) and IV:4 (14); and red/grey hexagons denote *LRAT*, P1 (27), P2 (54), and P3 (41). **(B)** Patient L-cone CFF data aligned with the normal L-cone template. Data for patient IV:4 with a defect in *OPN1LW/MW* is not shown because the CFF function comprised a single point for which a unique shift cannot be determined.

Figure 10.

Patient S-cone CFF data, using same symbol conventions as in Figures 8 and 9 (see key). Normal S-cone template shown in white. **(A)** All patient S-cone CFFs plotted on logarithmic axis as a function of log target radiance. **(B):** S-cone CFFs from **(A)** horizontally and vertically aligned with the normal S-cone template. ES5 (aged 28) and ES6 (aged 27) carried out only the S-cone measurements.

Figure 11.

Horizontal and vertical shifts required on double logarithmic co-ordinates to align the patient CFF functions (see key) with the normal template. **(A):** L-cone CFF functions. The shifts for normal observers (crosses) are roughly symmetrically placed about the origin. The diagonal dashed line with a slope of -0.26 Hz per $\log_{10}$ unit is the best fit to the cluster of patient points lying along the diagonal in upper left quadrant (> 0 Hz and < 0 $\log_{10}$ Td). **(B):** S-cone CFF functions.

References

Adelson, E.H., 1982. Saturation and adaptation in the rod system. Vision Res 22, 1299-1312.

Aguilar, M., Stiles, W.S., 1954. Saturation of the rod mechanism of the retina at high levels of stimulation. Optica Acta 1, 59-64.

Alexander, C., Votruba, M., Pesch, U.E., Thiselton, D.L., Mayer, S., Moore, A., Rodriguez, M., Kellner, U., Leo-Kottler, B., Auburger, G., Bhattacharya, S.S., Wissinger, B., 2000. OPA1, encoding a dynamin-related GTPase, is mutated in autosomal dominant optic atrophy linked to chromosome 3q28. Nat Genet 26, 211-215.

Alexander, K.R., Fishman, G.A., 1984. Rod-cone interaction in flicker perimetry. Brit J Ophthalmol 68, 303-309.

Arshavsky, V.Y., Lamb, T.D., Pugh, E.N., Jr., 2002. G proteins and phototransduction. Annual Review of Physiology 64, 153-187.

Ba-Abbad, R., 2018. Characterisation of temporal vision in congenital stationary night blindness, Institute of Ophthalmology. University College London, London.

Barlow, H.B., 1956. Retinal noise and absolute threshold. Journal of the Optical Society America 46, 634-639.

Barlow, H.B., 1972. Dark and light adaptation: Psychophysics, in: Jameson, D., Hurvich, L.M. (Eds.), Handbook of Sensory Physiology. Springer-Verlag, Berlin, pp. 1-28.

Barlow, H.B., Fitzhugh, R., Kuffler, S.W., 1957. Change of organization in the receptive fields of the cat's retina during dark adaptation. Journal of Physiology 137, 338-354.

Barlow, H.B., Levick, W.R., 1976. Threshold setting by the surround of cat retinal ganglion cells. Journal of Physiology 259, 737-757.

Batten, M.L., Imanishi, Y., Maeda, T., Tu, D.C., Moise, A.R., Bronson, D., Possin, D., Van Gelder, R.N., Baehr, W., Palczewski, K., 2004. Lecithin-retinol acyltransferase is essential for accumulation of all-trans-retinyl esters in the eye and in the liver. J Biol Chem 279, 10422-10432.

Berger, W., Kloeckener-Gruissem, B., Neidhardt, J., 2010. The molecular basis of human retinal and vitreoretinal diseases. Prog Retin Eye Res 29, 335-375.

Bills, M.A., 1920. The lag of visual sensation in its relation to wave lengths and intensity of light. Psychological review company, Princeton, N.J., Lancaster, Pa.,.

Burns, M.E., Baylor, D.A., 2001. Activation, deactivation and adaptation in vertebrate photoreceptor cells. Annual review of neuroscience 24, 779-805.

Burte, F., Carelli, V., Chinnery, P.F., Yu-Wai-Man, P., 2015. Disturbed mitochondrial dynamics and neurodegenerative disorders. Nature Reviews Neurology 11, 11-24.

Chan, L.-H., Freeman, A.W., Cleland, B.G., 1992. The rod-cone shift and its effect on ganglion cells in the cat's retina. Vision Res 32, 2209-2219.

Cleveland, W.S., 1979. Robust locally weighted regression and smoothing scatterplots. J Am Stat Assoc 74, 829-836.

Cohn, A.C., Toomes, C., Hewitt, A.W., Kearns, L.S., Inglehearn, C.F., Craig, J.E., Mackey, D.A., 2008. The natural history of OPA1-related autosomal dominant optic atrophy. Brit J Ophthalmol 92, 1333-1336.

Coletta, N.J., Adams, A.J., 1984. Rod-cone interaction in flicker detection. Vision Res 24, 1333-1340.

Collins, J.B., 1956. The influence of characteristics of a fluctuating visual stimulus on flicker sensation. Ophthalmologica 131, 83-104.

Conner, J.D., 1982. The temporal properties of rod vision. Journal of Physiology 332, 139-155.

Corwin, T.R., Dunlap, W.P., 1987. The shape of the high frequency flicker sensitivity curve. Vision Res 27, 2119-2123.

de Lange, H., 1958. Research into the dynamic nature of the human fovea-cortex systems with intermittent and modulated light. II. Phase shift in brightness and delay in color perception. J Opt Soc Am 48, 784-789.

Delettre, C., Lenaers, G., Griffoin, J.M., Gigarel, N., Lorenzo, C., Belenguer, P., Pelloquin, L., Grosgeorge, J., Turc-Carel, C., Perret, E., Astarie-Dequeker, C., Lasquellec, L., Arnaud, B., Ducommun, B., Kaplan, J., Hamel, C.P., 2000. Nuclear gene OPA1, encoding a mitochondrial dynamin-related protein, is mutated in dominant optic atrophy. Nat Genet 26, 207-210.

DevBorman, A., Ocaka, L.A., Mackay, D.S., Ripamonti, C., Henderson, R.H., Moradi, P., Hall, G., Black, G.C., Robson, A.G., Holder, G.E., Webster, A.R., Fitzke, F., Stockman, A., Moore, A.T., 2012. Early Onset Retinal Dystrophy Due to Mutations in LRAT: Molecular Analysis and Detailed Phenotypic Study. Invest Ophth Vis Sci 53, 3927-3938.

Dryja, T.P., McGee, T.L., Berson, E.L., Fishman, G.A., Sandberg, M.A., Alexander, K.R., Derlacki, D.J., Rajagopalan, A.S., 2005. Night blindness and abnormal cone electroretinogram ON responses in patients with mutations in the GRM6 gene encoding mGluR6. Proceedings of the National Academy of Science U.S.A. 102, 4884-4889.

Dunn, F.A., Lankheet, M.J., Rieke, F., 2007. Light adaptation in cone vision involves switching between receptor and post-receptor sites. Nature 449, 603-607.

Estevez, O., Cavonius, C.R., 1975. Flicker sensitivity of the human red and green color mechanisms. Vision Res 15, 879-881.

Fain, G.L., Matthews, H.R., Cornwall, M.C., Koutalos, Y., 2001. Adaptation in vertebrate photoreceptors. Physiological Reviews 80, 117-151.

Fan, J., Rohrer, B., Frederick, J.M., Baehr, W., Crouch, R.K., 2008. Rpe65-/- and Lrat-/- mice: comparable models of leber congenital amaurosis. Investigative Ophthalmol & Visual Science 49, 2384-2389.

Ferry, E.S., 1892. Persistence of vision. American Journal of Science 44, 192-207.

Frumkes, T.E., Eysteinsson, T., 1988. The cellular basis for suppressive rod-cone interaction. Visual Neurosci 1, 263-273.

Gardner, J.C., Webb, T.R., Kanuga, N., Robson, A.G., Holder, G.E., Stockman, A., Ripamonti, C., Ebenezer, N.D., Ogun, O., Devery, S., Wright, G.A., Maher, E.R., Cheetham, M.E., Moore, A.T., Michaelides, M., Hardcastle, A.J., 2010. X-linked cone dystrophy (XLCOD5) caused by mutation of the red and green cone opsins. Am J Hum Genet 87, 26-39.

Gibson, J.J., Waddell, D., 1952. Homogeneous retinal stimulation and visual perception. The American Journal of Psychology 65, 263-270.

Ginsburg, N., 1966. Local adaptation to intermittent light as a function of frequency and eccentricity. American Journal of Psychology 79, 296-300.

Giorgi, A., 1963. Effect of wavelength on the relationship between critical flicker frequency and intensity in foveal vision. J Opt Soc Am 53, 480-486.

Goldberg, S.H., Frumkes, T.E., Nygaard, R.W., 1983. Inhibitory influence of unstimulated rods in the human retina: evidence provided by examining cone flicker. Science 221, 180-182.

Greenstein, V.C., Zaidi, Q., Hood, D.C., Spehar, B., Cideciyan, A.V., Jacobson, S.G., 1996. The enhanced S cone syndrome: an analysis of receptoral and post-receptoral changes. Vision Res 36, 3711-3722.

Gu, S.M., Thompson, D.A., Srikumari, C.R., Lorenz, B., Finckh, U., Nicoletti, A., Murthy, K.R., Rathmann, M., Kumaramanickavel, G., Denton, M.J., Gal, A., 1997. Mutations in *RPE65* cause autosomal recessive childhood-onset severe retinal dystrophy. Nat Genet 17, 194-197.

Haider, N.B., Jacobson, S.G., Cideciyan, A.V., Swiderski, R., Streb, L.M., Searby, C., Beck, G., Hockey, R., Hanna, D.B., Gorman, S., Duhl, D., Carmi, R., Bennett, J., Weleber, R.G., Fishman, G.A., Wright, A.F., Stone, E.M., Sheffield, V.C., 2000. Mutation of a nuclear receptor gene, NR2E3, causes enhanced S cone syndrome, a disorder of retinal cell fate. Nat Genet 24, 127-131.

Hamer, R.D., Tyler, C.W., 1992. Analysis of visual modulation sensitivity. V. Faster visual response for G- than for R-cone pathway? J. Opt. Soc. Am. A 9, 1889-1904.

Hanein, S., Perrault, I., Gerber, S., Tanguy, G., Barbet, F., Ducroq, D., Calvas, P., Dollfus, H., Hamel, C.P., Lopponen, T., Munier, F., Santos, L., Shalev, S., Zafeirou, D., Dufier, J.L., Munnich, A., Rozet, J.M., Kaplan, J., 2004. Leber congenital amaurosis: comprehensive survey of the genetic heterogeneity, refinement of the clinical definition, and genotype-phenotype correlations as a strategy for molecular diagnosis. Hum Mutat 23, 306-317.

Hecht, S., Shlaer, S., 1936. Intermittent stimulation by light. V. The relation between intensity and critical frequency for different parts of the spectrum. J Gen Physiol 19, 965-977.

Hecht, S., Verrijp, C.D., 1933a. The influence of intensity, color and retinal location on the fusion frequency of intermittent illumination. Proceedings of the National Academy of Sciences of the United States of America 19, 522-535.

Hecht, S., Verrijp, C.D., 1933b. Intermittent stimulation by light. III. The relation between intensity and critical fusion frequency for different retinal locations. J Gen Physiol 17, 251-268.

Hood, D.C., Cideciyan, A.V., Román, A.J., Jacobson, S.G., 1995. Enhanced S cone syndrome: evidence for an abnormally large number of S cones. Vision Res 35, 1473-1481.

Ives, H.E., 1912. Studies in the photometry of lights of different colours. II. Spectral luminosity curves by the method of critical frequency. Philos Mag 24, 352-370.

Jacobson, S.G., Marmor, M.F., Kemp, C.M., Knighton, R.W., 1990. SWS (blue) cone hypersensitivity in a newly identified retinal degeneration. Investigative Ophthalmololy & Visual Science 31, 827-838.

Johnston, P.B., Gaster, R.N., Smith, V.C., Tripathi, R.C., 1979. A clinicopathologic study of autosomal dominant optic atrophy. Am J Ophthalmol 88, 868-675.

Kellner, U., Zrenner, E., Sadowski, B., Foerster, M.H., 1993. Enhanced S cone sensitivity syndrome: long-term follow-up, electrophysiological and psychophysical findings. Clin Vision Sci 8, 425-434.

Kelly, D.H., 1961. Visual responses to time-dependent stimuli I. Amplitude sensitivity measurements. J Opt Soc Am 51, 422-429.

Kelsell, R.E., Gregory-Evans, K., Payne, A.M., Perrault, I., Kaplan, J., Yang, R.B., Garbers, D.L., Bird, A.C., Moore, A.T., Hunt, D.M., 1998. Mutations in the retinal guanylate cyclase (RETGC-1) gene in dominant cone-rod dystrophy. Hum Mol Genet 7, 1179-1184.

Kjer, P., 1959. Infantile optic atrophy with dominant mode of inheritance: a clinical and genetic study of 19 Danish families. Acta Ophthalmologica Supplement 164, 1-147.

Kjer, P., Jensen, O.A., Klinken, L., 1983. Histopathology of eye, optic nerve and brain in a case of dominant optic atrophy. Acta Ophthalmol 61, 300-312.

Kohlrausch, A., 1922. Untersuchungen mit farbingen Schwellprüflichtern über den Dunkeladaptationsuerlauf des normalen Auges. Pflügers Archiv für die Gesamte Physiologie des Menschen und der Tiere 196, 113-117.

Krauskopf, J., Mollon, J.D., 1971. The independence of the temporal integration properties of individual chromatic mechanisms in the human eye. Journal of Physiology 219, 611-623.

Landis, C., 1954. Determinants of the critical flicker-fusion threshold. Physiological Reviews 34, 259-286.

MacLeod, D.I.A., 1978. Visual sensitivity. Annual Review of Psychology 29, 613-645.

Majander, A., João, C., Rider, A.T., Henning, G.B., Votruba, M., Moore, A.T., Yu-Wai-Man, P., Stockman, A., 2017. The pattern of retinal ganglion cell loss in *OPA1*-related autosomal dominant optic atrophy inferred from temporal, spatial, and chromatic sensitivity losses. Invest Ophth Vis Sci 58, 502-516.

Marlhens, F., Bareil, C., Griffoin, J.M., Zrenner, E., Amalric, P., Eliaou, C., Liu, S.Y., Harris, E., Redmond, T.M., Arnaud, B., Claustres, M., Hamel, C.P., 1997. Mutations in *RPE65* cause Leber's congenital amaurosis. Nat Genet 17, 139-141.

Marmor, M.F., Jacobson, S.G., Forester, M.H., Kellner, U., Weleber, R.G., 1990. Diagnostic findings of a new syndrome with night blindness, maculopathy, and enhanced S cone sensitivity. Am J Ophthalmol 110, 124-134.

Milam, A.H., Rose, L., Cideciyan, A.V., Barakat, M.R., Tang, W.-X., Gupta, N., Aleman, T.S., Wright, A.F., Stone, E.M., Sheffield, V.C., Jacobson, S.G., 2002. The nuclear receptor NR2E3 plays a role in human retinal photoreceptor differentiation and degeneration. Proceedings of the National Academy of Sciences 99, 473-478.

Mollon, J.D., Polden, P.G., 1977. Saturation of a retinal cone mechanism. Nature 259, 243-246.

Mukherjee, R., Robson, A.G., Holder, G.E., Stockman, A., Egan, C.A., Moore, A.T., Webster, A.R., 2014. A detailed phenotypic description of autosomal dominant cone dystrophy due to a *de novo* mutation in the *GUCY2D* gene. Eye 28, 481-487.

Nakajima, Y., Iwakabe, H., Akazawa, C., Nawa, H., Shigemoto, R., Mizuno, N., Nakanishi, S., 1993. Molecular characterization of a novel retinal metabotropic glutamate receptor

mGluR6 with a high agonist selectivity for L-2-amino-4-phosphonobutyrate. J Biol Chem 268, 11868-11873.

Nishiguchi, K.M., Sandberg, M.A., Kooijman, A.C., Martemyanov, K.A., Pott, J.W.R., Hagstrom, S.A., Arshavsky, V.Y., Berson, E.L., Dryja, T.P., 2004. Defects in RGS9 or its anchor protein R9AP in patients with slow photoreceptor deactivation. Nature 427, 75-78.

O'Connor, E., Allen, L.E., Bradshaw, K., Boylan, J., Moore, A.T., Trump, D., 2006. Congenital stationary night blindness associated with mutations in GRM6 encoding glutamate receptor MGluR6. Brit J Ophthalmol 90, 653-654.

Payne, A.M., Downes, S.M., Bessant, D.A., Taylor, R., Holder, G.E., Warren, M.J., Bird, A.C., Bhattacharya, S.S., 1998. A mutation in guanylate cyclase activator 1A (GUCA1A) in an autosomal dominant cone dystrophy pedigree mapping to a new locus on chromosome 6p21.1. Hum Mol Genet 7, 273-277.

Perlman, I., Normann, R.A., 1998. Light adaptation and sensitivity controlling mechanisms in vertebrate photoreceptors. Prog Retin Eye Res 17, 523-563.

Perrault, I., Rozet, J.M., Gerber, S., Ghazi, I., Leowski, C., Ducroq, D., Souied, E., Dufier, J.L., Munnich, A., Kaplan, J., 1999a. Leber congenital amaurosis. Molecular Genetics and Metabolism 68, 200-208.

Perrault, I., Rozet, J.M., Ghazi, I., Leowski, C., Bonnemaison, M., Gerber, M., Ducroq, D., Cabot, A., Souied, E., Dufier, J.L., Pittler, S., Munnich, A., Kaplan, J., 1999b. Different functional outcome of retGC1 and RPE65 gene mutations in Leber congenital amaurosis. Am J Hum Genet 64, 1225-1228.

Piéron, H., 1922. L'influence de l'intensité lumineuse sur la persistance rétinienne apparente. Archives Néerlandaises de Physiologie de l'homme et des animaux VII, 199-212.

Plateau, J., 1829. Dissertation sur quelques propriétés des impressions produites par Ia Iumière sur l'organe de Ia vue Dessain, Liège.

Pokorny, J., Smith, V.C., 1972. Luminosity and CFF in deuteranopes and protanopes. J Opt Soc Am 62, 111-117.

Porter, T.C., 1902. Contributions to the study of flicker. Paper II. P R Soc London 70, 313-329.

Pugh, E.N., Jr., Lamb, T.D., 2000. Phototransduction in vertebrate rods and cones: molecular mechanisms of amplification, recovery and light adaptation, in: Stavenga, D.G., de Grip, W.J., Pugh, E.N. (Eds.), Handbook of biological physics, Vol. 3, Molecular mechanisms of visual transduction. Elsevier, Amsterdam, pp. 183-255.

Pugh, E.N., Jr., Nikonov, S., Lamb, T.D., 1999. Molecular mechanisms of vertebrate photoreceptor light adaptation. Current Opinion in Neurobiology 9, 410-418.

Pulfrich, C., 1922. Die Stereskopie im Dienste der isochromen und heterochromen Photometrie. Naturwissenschaften 10, 553-564.

Raninen, A., Franssila, R., Rovamo, J., 1991. Critical flicker frequency to red targets as a function of luminance and flux across the human visual field. Vision Res 31, 1875-1881.

Redmond, T.M., Yu, S., Lee, E., Bok, D., Hamasaki, D., Chen, N., Goletz, P., Ma, J.X., Crouch, R.K., Pfeifer, K., 1998. *Rpe65* is necessary for production of 11-*cis*-vitamin A in the retinal visual cycle. Nat Genet 20, 344-351.

Rider, A.T., Henning, G.B., Stockman, A., 2019. Light adaptation controls visual sensitivity by adjusting the speed and gain of the response to light. Plos One 14, e0220358.

Ripamonti, C., Aboshiha, J., Henning, G.B., Sergouniotis, I.P., Michaelides, M., Moore, A.T., Webster, A., Stockman, A., 2014a. Vision in observers with enhanced S-cone syndrome: an excess of S-cones but connected mainly to conventional S-cone pathways. Investigative Ophthalmology and Visual Science 55, 963-976.

Ripamonti, C., Henning, G.B., Ali, R.R., Bainbridge, J.W.B., Robbie, S.J., Sundaram, V., Luong, V.A., van den Born, L.I., Casteels, I., de Ravel, T.J.L., Moore, A.T., Stockman, A., 2014b. Nature of the visual loss in observers with Leber's congenital amaurosis caused by specific mutations in RPE65. Invest Ophth Vis Sci 55, 6817-6828.

Rogers, B.J., Anstis, S.M., 1972. Intensity versus adaptation and the Pulfrich stereophenomenon. Vision Res 12, 909-928.

Ruiz, A., Winston, A., Lim, Y.H., Gilbert, B.A., Rando, R.R., Bok, D., 1999. Molecular and biochemical characterization of lecithin retinol acyltransferase. J Biol Chem 274, 3834-3841.

Salah, S.B., Kamei, S., Sénéćhal, A., Lopez, S., Bazalgette, C., Bazalgette, C., Eliaou, C.M., Zanlonghi, X., Hamel, C.P., 2008. Novel *KCNV2* mutations in cone dystrophy with supernormal rod electroretinogram. Am J Ophthalmol 145, 1099-1106.

Senechal, A., Humbert, G., Surget, M.O., Bazalgette, C., Bazalgette, C., Arnaud, B., Arndt, C., Laurent, E., Brabet, P., Hamel, C.P., 2006. Screening genes of the retinoid metabolism: novel LRAT mutation in leber congenital amaurosis. Am J Ophthalmol 142, 702-704.

Sergouniotis, P.I., Robson, A.G., Li, Z., Devery, S., Holder, G.E., Moore, A.T., Webster, A.R., 2012. A phenotypic study of congenital stationary night blindness (CSNB) associated with mutations in the GRM6 gene. Acta Ophthalmol 90, e192-197.

Shapley, R., 2009. Linear and nonlinear systems analysis of the visual system: why does it seem so linear? A review dedicated to the memory of Henk Spekreijse. Vision Res 49, 907-921.

Shapley, R., Enroth-Cugell, C., 1984. Visual Adaptation and Retinal Gain Controls. Progress in Retinal Research 3, 263-346.

Sharon, D., Sandberg, M.A., Caruso, R.C., Berson, E.L., Dryja, T.P., 2003. Shared mutations in NR2E3 in enhanced S-cone syndrome, Goldmann-Favre syndrome, and many cases of clumped pigmentary retinal degeneration. Arch Ophthalmol-Chic 121, 1316-1323.

Simonson, E., Brožek, J., 1952. Flicker fusion frequency: background and applications. Physiological Reviews 32, 349-378.

Smithson, H.E., 2014. S-cone psychophysics. Visual Neurosci 31, 211-225.

Stockman, A., Henning, G.B., Michaelides, M., Moore, A.T., Webster, A., Cammack, J., Ripamonti, C., 2014a. Cone dystrophy with “supernormal” rod ERG: psychophysical testing shows comparable rod and cone temporal sensitivity losses with no gain in rod function. Invest Ophth Vis Sci 55, 832-840.

Stockman, A., Henning, G.B., Moore, A.T., Webster, A.R., Michaelides, M., Ripamonti, C., 2014b. Visual consequences of molecular changes in the guanylate cyclase activating protein. Invest Ophth Vis Sci 55, 1930-1940.

Stockman, A., Henning, G.B., Rider, A.T., 2021. Clinical vision and molecular loss: Integrating visual psychophysics with molecular genetics reveals key details of normal and abnormal visual processing. Prog Retin Eye Res 83, 100937.

Stockman, A., Langendörfer, M., Smithson, H.E., Sharpe, L.T., 2006. Human cone light adaptation: from behavioral measurements to molecular mechanisms. J Vision 6, 1194-1213.

Stockman, A., MacLeod, D.I.A., DePriest, D.D., 1991. The temporal properties of the human short-wave photoreceptors and their associated pathways. Vision Res 31, 189-208.

Stockman, A., Mollon, J.D., 1986. The spectral sensitivities of the middle- and long-wavelength cones: an extension of the two-colour threshold technique of W S. Stiles. Perception 15, 729-754.

Stockman, A., Plummer, D.J., 1998. Color from invisible flicker: a failure of the Talbot-Plateau law caused by an early "hard" saturating nonlinearity used to partition the human short-wave cone pathway. Vision Res 38, 3703-3728.

Stockman, A., Sharpe, L.T., 2000. Spectral sensitivities of the middle- and long-wavelength sensitive cones derived from measurements in observers of known genotype. Vision Res 40, 1711-1737.

Stockman, A., Sharpe, L.T., Fach, C.C., 1999. The spectral sensitivity of the human short-wavelength cones. Vision Res 39, 2901-2927.

Stockman, A., Sharpe, L.T., Tufail, A., Kell, P.D., Ripamonti, C., Jeffery, G., 2007a. The effect of sildenafil citrate (Viagra®) on visual sensitivity. J Vision 7(8):4, 4, 1-15.

Stockman, A., Smithson, H.E., Michaelides, M., Moore, A.T., Webster, A.R., Sharpe, L.T., 2007b. Residual cone vision without α-transducin. J Vision 7, 8.1-13.

Stockman, A., Smithson, H.E., Webster, A.R., Holder, G.E., Rana, N.A., Ripamonti, C., Sharpe, L.T., 2008. The loss of the PDE6 deactivating enzyme, RGS9, results in precocious light adaptation at low light levels. J Vision 8, 10.11-10.

Thiagalingam, S., McGee, T.L., Sandberg, M.A., Trzupek, K.M., Berson, E.L., Dryja, T.P., 2007. Novel mutations in the *KCNV2* gene in patients with cone dystrophy and a supernormal rod electroretinogram. Ophthalmic Genet 28, 135-142.

Thoreson, W.B., Mangel, S.C., 2012. Lateral interactions in the outer retina. Prog Retin Eye Res 31, 407-441.

Tyler, C.W., Hamer, R.D., 1990. Analysis of visual modulation sensitivity. IV. Validity of the Ferry-Porter law. J. Opt. Soc. Am. A 7, 743-758.

Tyler, C.W., Hamer, R.D., 1993. Eccentricity and the Ferry-Porter law. J. Opt. Soc. Am. A 10, 2084-2087.

Votruba, M., Fitzke, F.W., Holder, G.E., Carter, A., Bhattacharya, S.S., Moore, A.T., 1998. Clinical features in affected individuals from 21 pedigrees with dominant optic atrophy. Arch Ophthalmol-Chic 116, 351-358.

Wald, G., 1945. Human vision and the spectrum. Science 101, 653-658.

Wang, J.-S., Kefalov, V.J., 2011. The cone-specific visual cycle. Prog Retin Eye Res 30, 115-128.

Westheimer, G., 1966. The Maxwellian view. Vision Res 6, 669-682.

Wilkie, S.E., Newbold, R.J., Deery, E., Walker, C.E., Stinton, I., Ramamurthy, V., Hurley, J.B., Bhattacharya, S.S., Warren, M.J., Hunt, D.M., 2000. Functional characterization of missense mutations at codon 838 in retinal guanylate cyclase correlates with disease severity in patients with autosomal dominant cone-rod dystrophy. Hum Mol Genet 9, 3065-3073.

Wissinger, B., Dangel, S., Jägle, H., Hansen, L., Baumann, B., Rudolph, G., Wolf, C., Bonin, M., Koeppen, K., Ladewig, T., Kohl, S.h., Zrenner, E., Rosenberg, T., 2008. Cone dystrophy with supernormal rod response is strictly associated with mutations in KCNV2. Investigative Ophthalmology and Visual Science 49, 751-757.

Wu, B.X., Moiseyev, G., Chen, Y., Rohrer, B., Crouch, R.K., Ma, J.X., 2004. Identification of RDH10, an all-trans retinol dehydrogenase, in retinal Muller cells. Invest Ophth Vis Sci 45, 3857-3862.

Wu, H., Cowing, J.A., Michaelides, M., Wilkie, S.E., Jeffery, G., Jenkins, S.A., Mester, V., Bird, A.C., Robson, A.G., Holder, G.E., Moore, A.T., Hunt, D.M., Webster, A.R., 2006. Mutations in the gene *KCNV2* encoding a voltage-gated Potassium channel subunit cause “cone dystrophy with supernormal rod electroretinogram” in humans. Am J Hum Genet 79, 574-579.

Yagasaki, K., Miyake, Y., Awaya, S., Ichikawa, H., 1986. ERG (electroretinogram) in hereditary optic atrophies. Nippon Ganka Gakkai Zasshi 90, 124-130.

Yu-Wai-Man, P., Griffiths, P.G., Burke, A., Sellar, P.W., Clarke, M.P., Gnanaraj, L., Ah-Kine, D., Hudson, G., Czermin, B., Taylor, R.W., Horvath, R., Chinnery, P.F., 2010. The prevalence and natural history of dominant optic atrophy due to OPA1 mutations. Ophthalmology 117, 1538-1546,.

Zeitz, C., Forster, U., Neidhardt, J., Feil, S., Kalin, S., Leifert, D., Flor, P.J., Berger, W., 2007. Night blindness-associated mutations in the ligand-blinding, cysteline-rich, and intracellular domains of the metabotroplic glutamate receptor 6 abolish protein trafficking. Hum Mutat 28, 771-780.

Znoiko, S.L., Crouch, R.K., Moiseyev, G., Ma, J.X., 2002. Identification of the RPE65 protein in mammalian cone photoreceptors. Invest Ophth Vis Sci 43, 1604-1609.

FIGURE 1

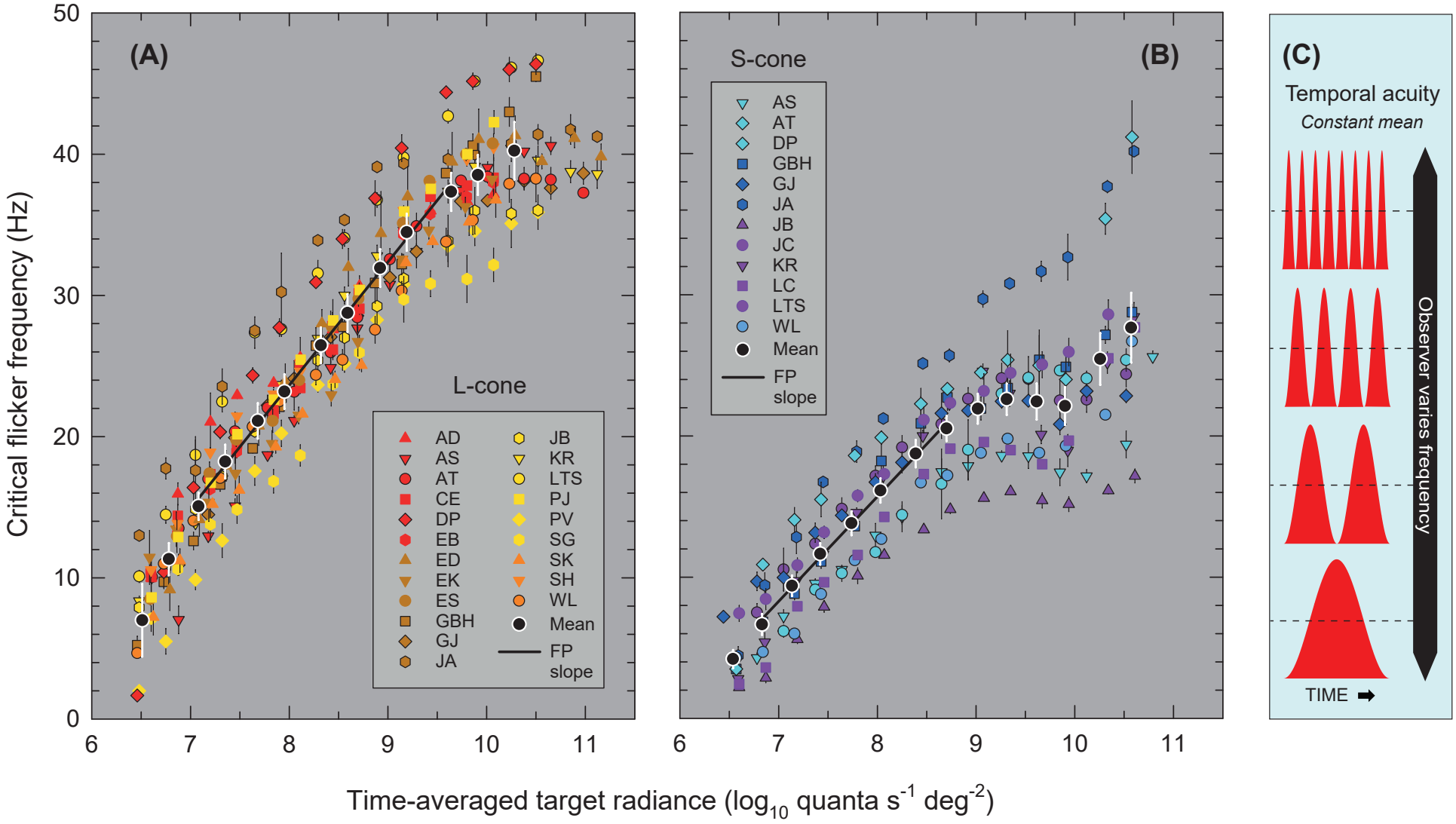
(A)
L-cone
AD
AS
AT
CE
DP
EB
ED
EK
ES
GBH
GJ
JA
JB
KR
LTS
PJ
PV
SG
SK
SH
WL
Mean
FP slope
(B)
S-cone
AS
AT
DP
GBH
GJ
JA
JB
JC
KR
LC
LTS
WL
Mean
FP slope
(C)
Temporal acuity
Constant mean
Observer varies frequency
TIME
Critical flicker frequency (Hz)
Time-averaged target radiance (log10 quanta s-1 deg-2)

FIGURE 2

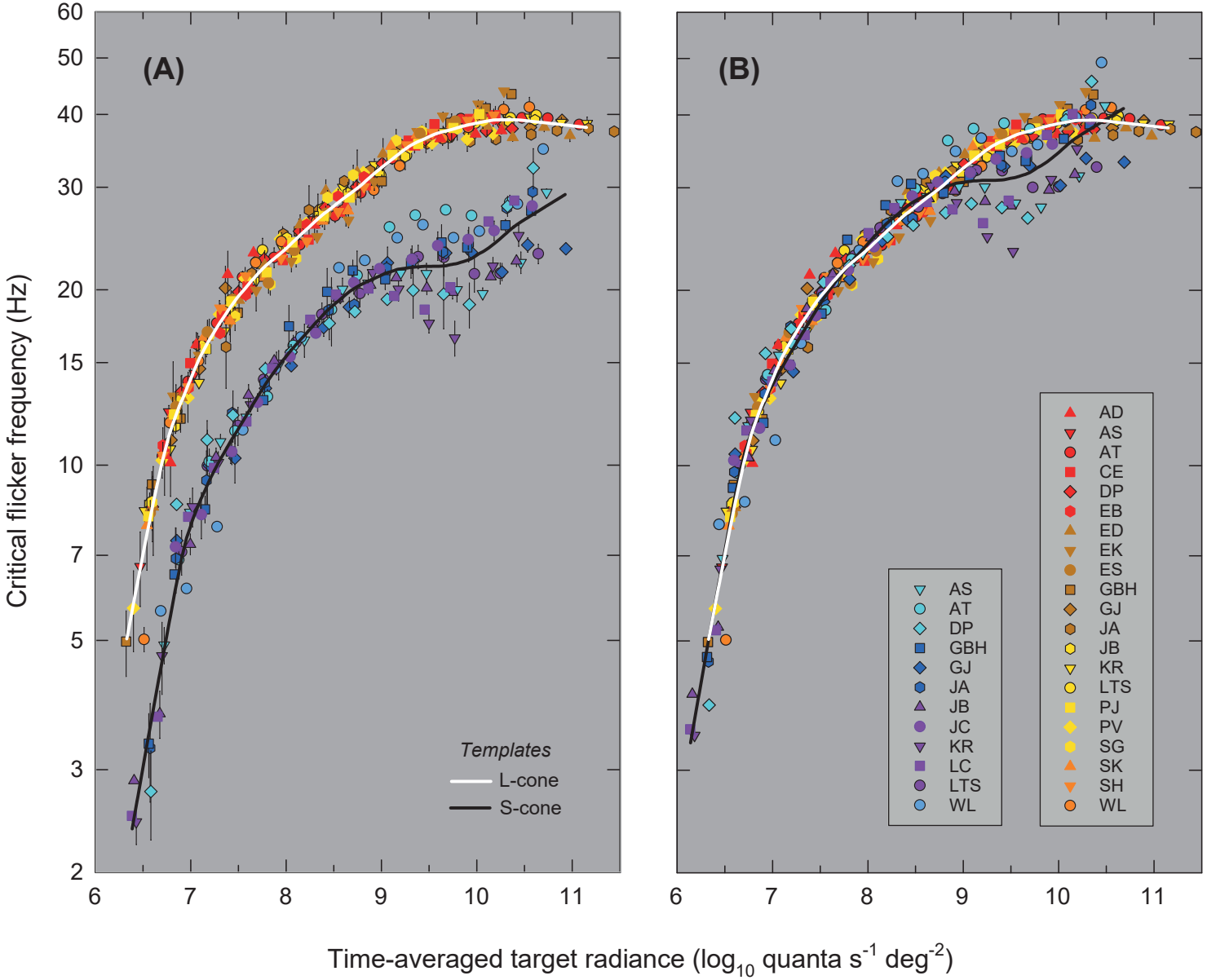
(A)
(B)
Critical flicker frequency (Hz)
60
50
40
30
20
15
10
7
5
3
2
6
7
8
9
10
11
Templates
L-cone
S-cone
AS
AT
DP
GBH
GJ
JA
JB
JC
KR
LC
LTS
WL
AD
AS
AT
CE
DP
EB
ED
EK
ES
GBH
GJ
JA
JB
KR
LTS
PJ
PV
SG
SK
SH
WL
Time-averaged target radiance (log_{10} quanta s^{-1} deg^{-2})

FIGURE 3

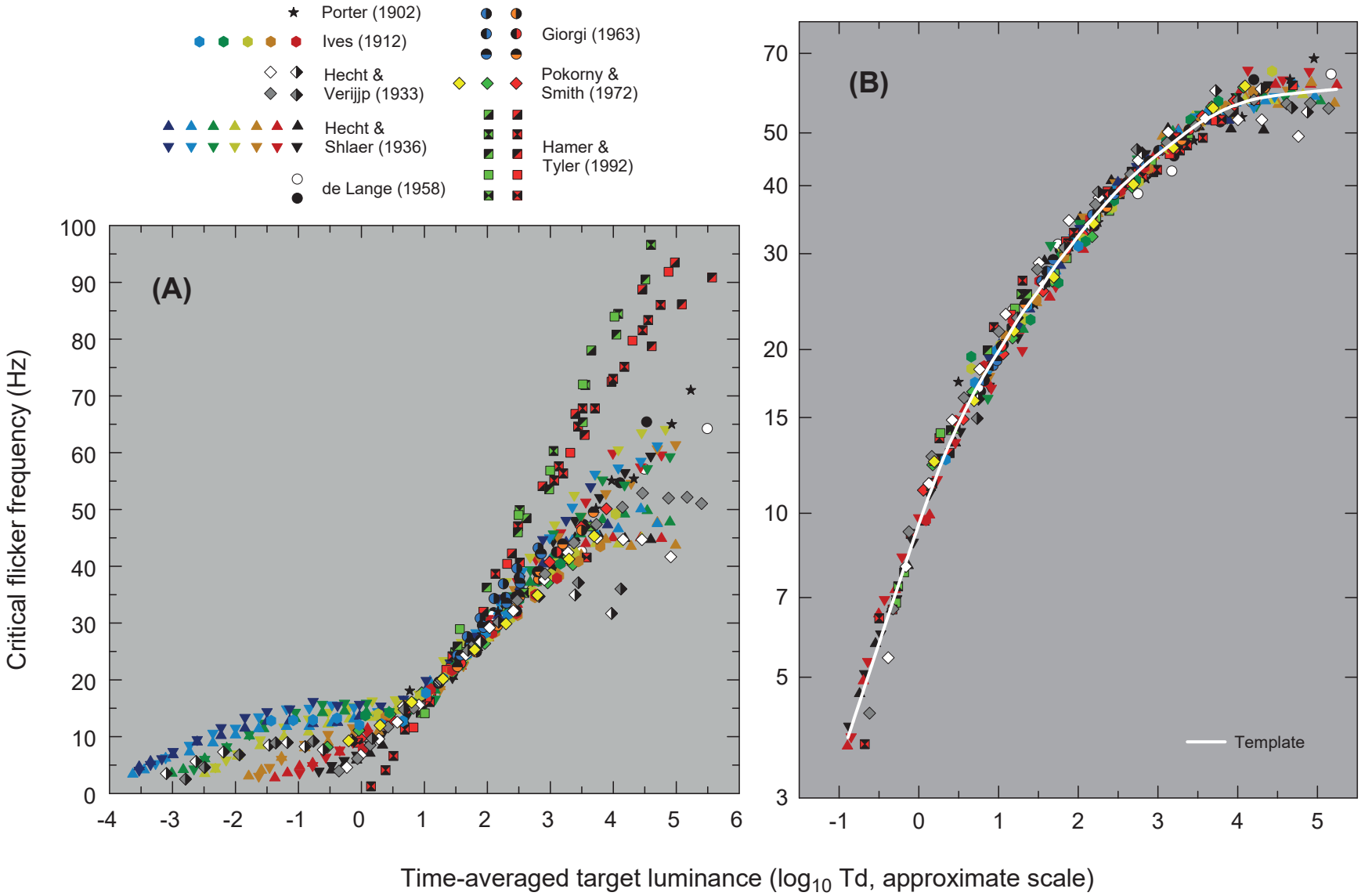
Porter (1902)
Ives (1912)
Hecht & Verijjp (1933)
Hecht & Shlaer (1936)
de Lange (1958)
Giorgi (1963)
Pokorny & Smith (1972)
Hamer & Tyler (1992)
(A)
(B)
Template
Critical flicker frequency (Hz)
Time-averaged target luminance (log10 Td, approximate scale)

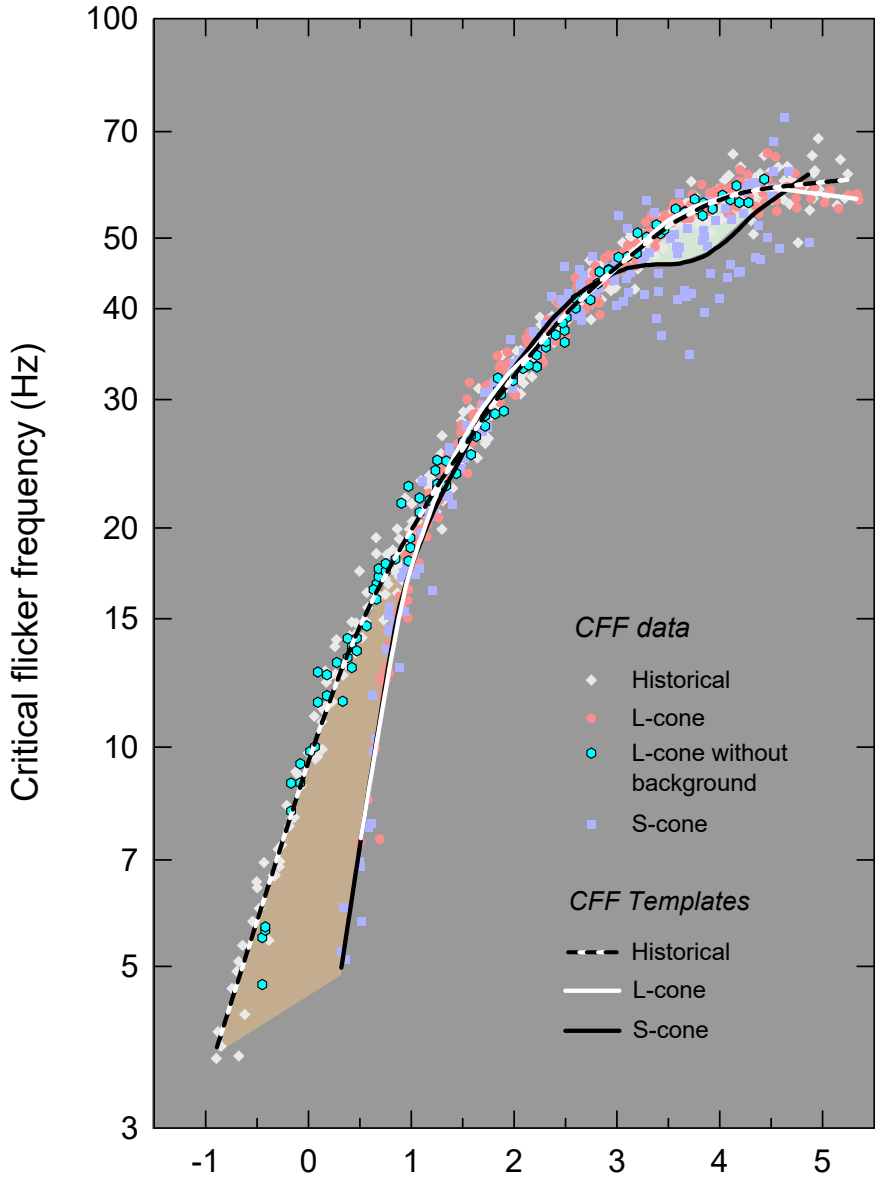

Time-averaged target luminance ($\log_{10}$ Td, approximate scale)

SEQUENTIAL MODEL

MODEL PARAMETERS

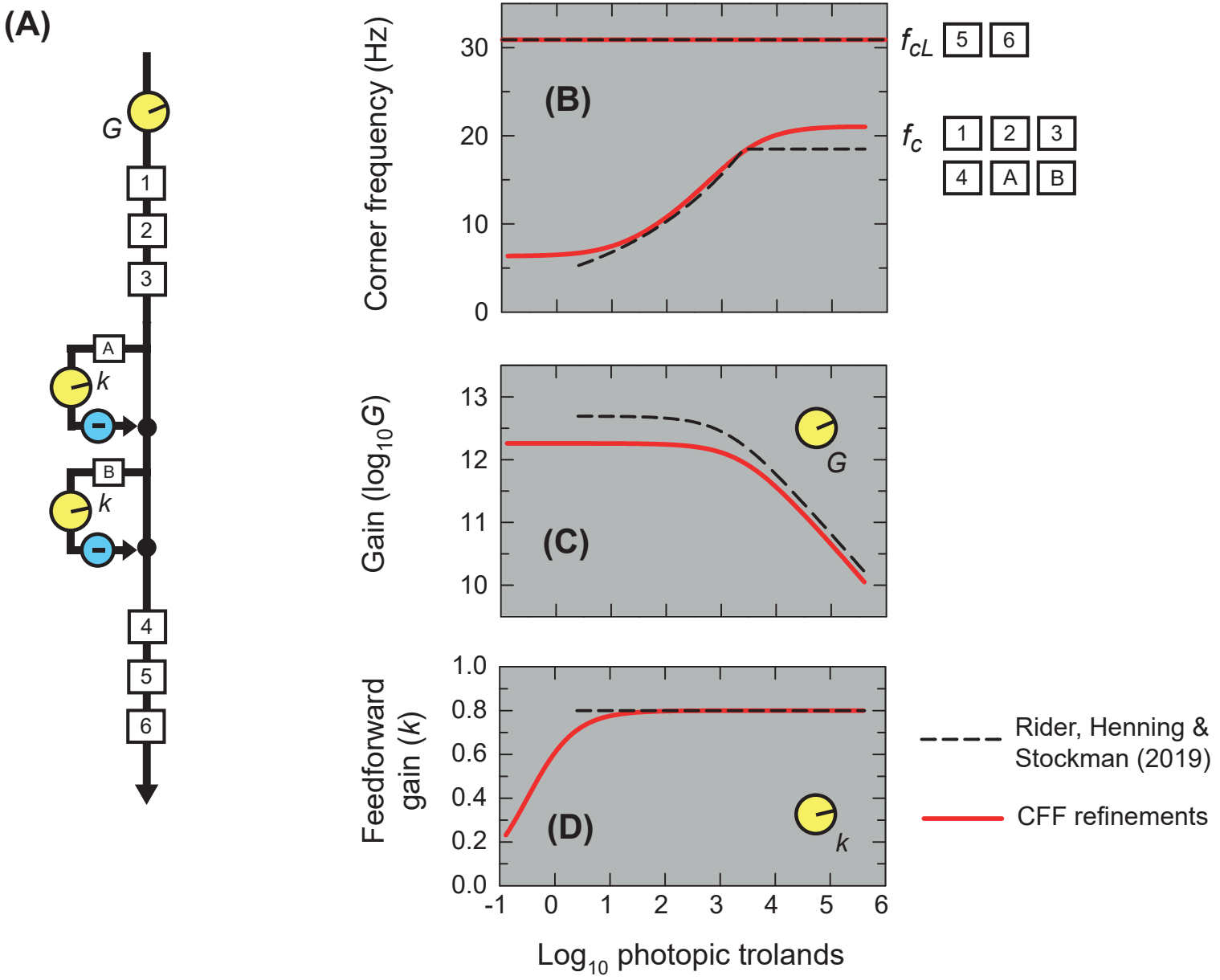

FIGURE 6

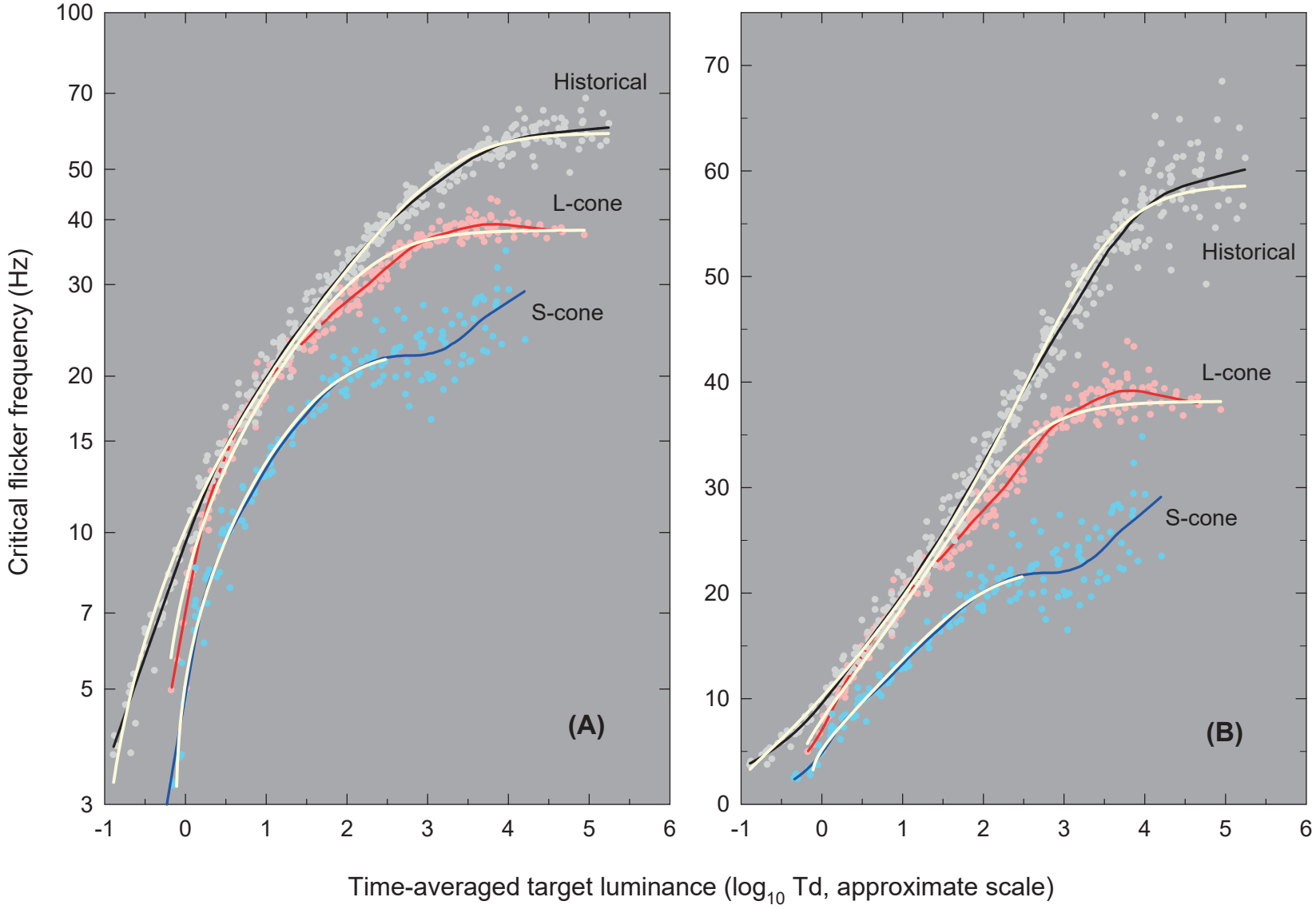
Critical flicker frequency (Hz)
100
70
50
40
30
20
15
10
7
5
3
-1
0
1
2
3
4
5
6
Historical
L-cone
S-cone
(A)
70
60
50
40
30
20
10
0
-1
0
1
2
3
4
5
6
Historical
L-cone
S-cone
(B)
Time-averaged target luminance (log10 Td, approximate scale)

FIGURE 7

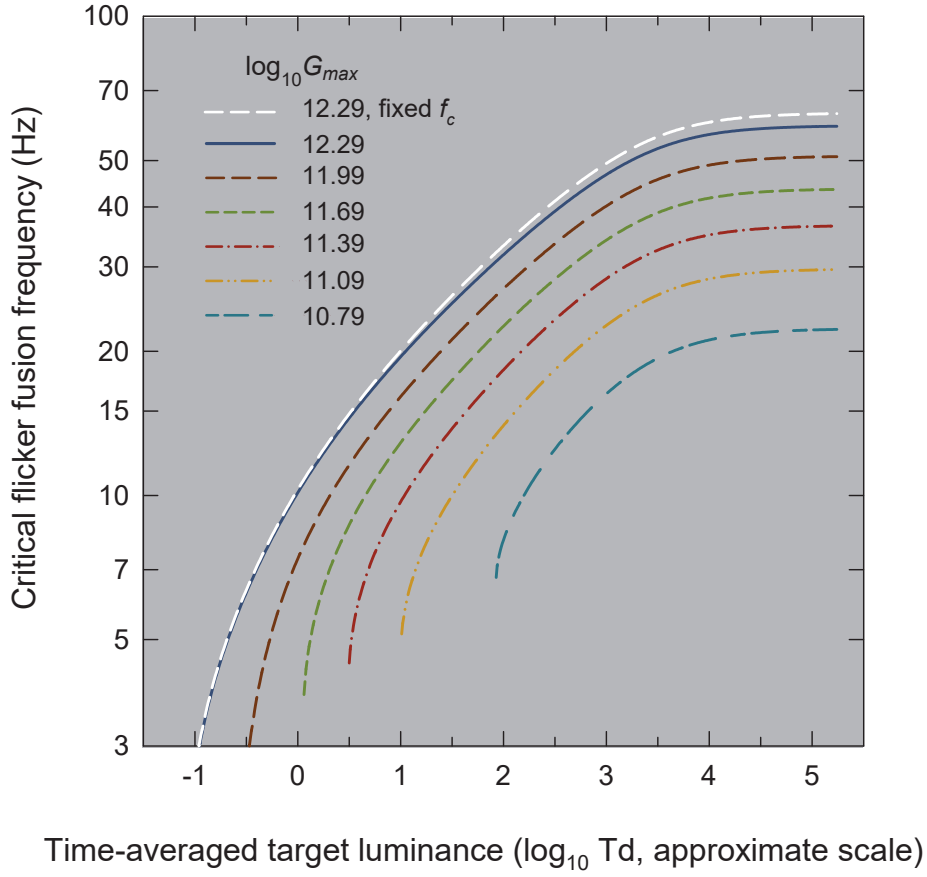
Critical flicker fusion frequency (Hz)
100
70
50
40
30
20
15
10
7
5
3
-1
0
1
2
3
4
5
log10Gmax
12.29, fixed fc
12.29
11.99
11.69
11.39
11.09
10.79
Time-averaged target luminance (log10 Td, approximate scale)

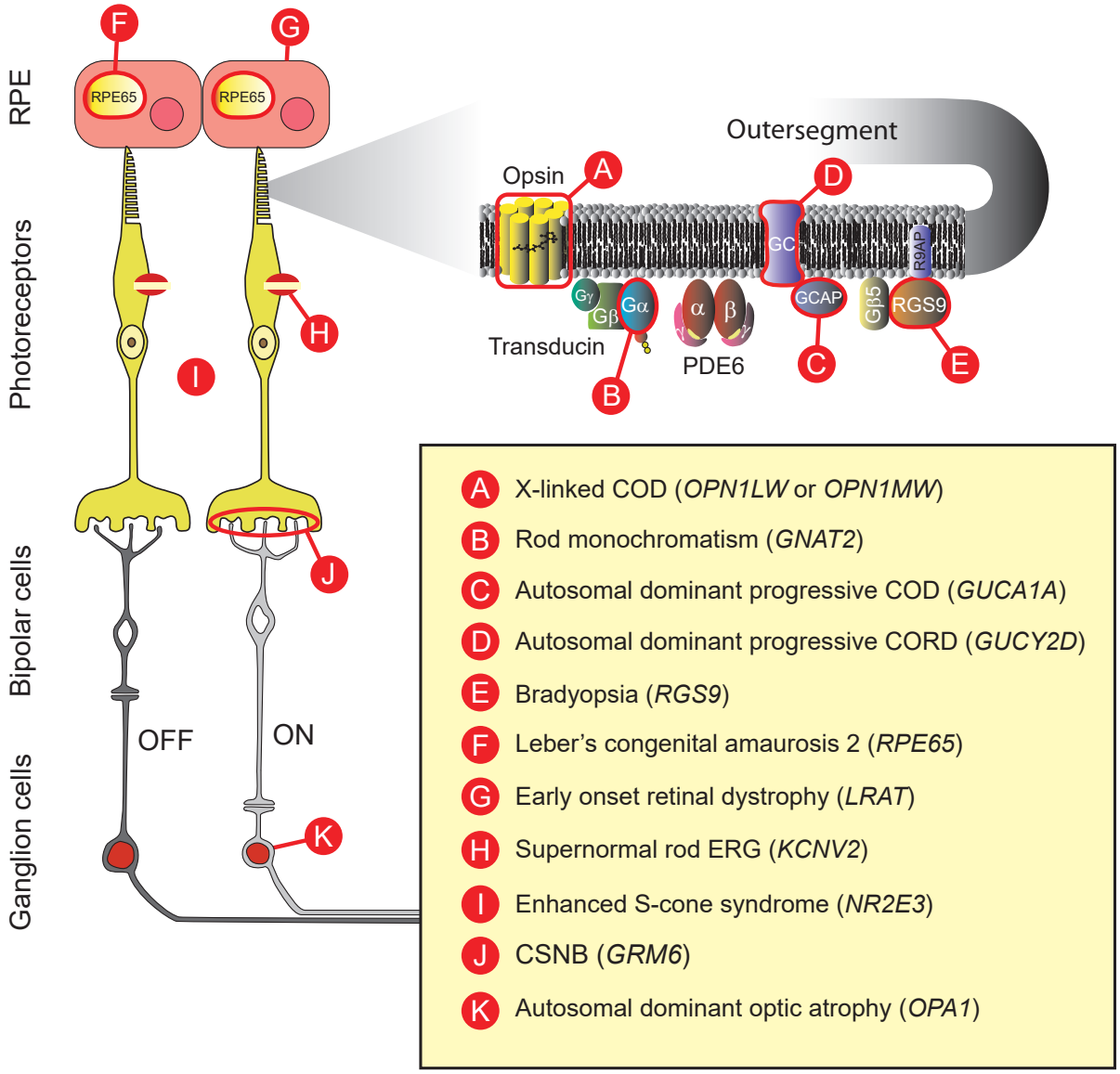
RPE
Photoreceptors
Bipolar cells
Ganglion cells
RPE65
RPE65
F
G
H
I
J
K
OFF
ON
Outersegment
Opsin
A
D
GC
R9AP
Gγ
Gβ
Gα
α
β
GCAP
Gβ5
RGS9
Transducin
PDE6
B
C
E
A X-linked COD (OPN1LW or OPN1MW)
B Rod monochromatism (GNAT2)
C Autosomal dominant progressive COD (GUCA1A)
D Autosomal dominant progressive CORD (GUCY2D)
E Bradyopsia (RGS9)
F Leber's congenital amaurosis 2 (RPE65)
G Early onset retinal dystrophy (LRAT)
H Supernormal rod ERG (KCNV2)
I Enhanced S-cone syndrome (NR2E3)
J CSNB (GRM6)
K Autosomal dominant optic atrophy (OPA1)

FIGURE 9

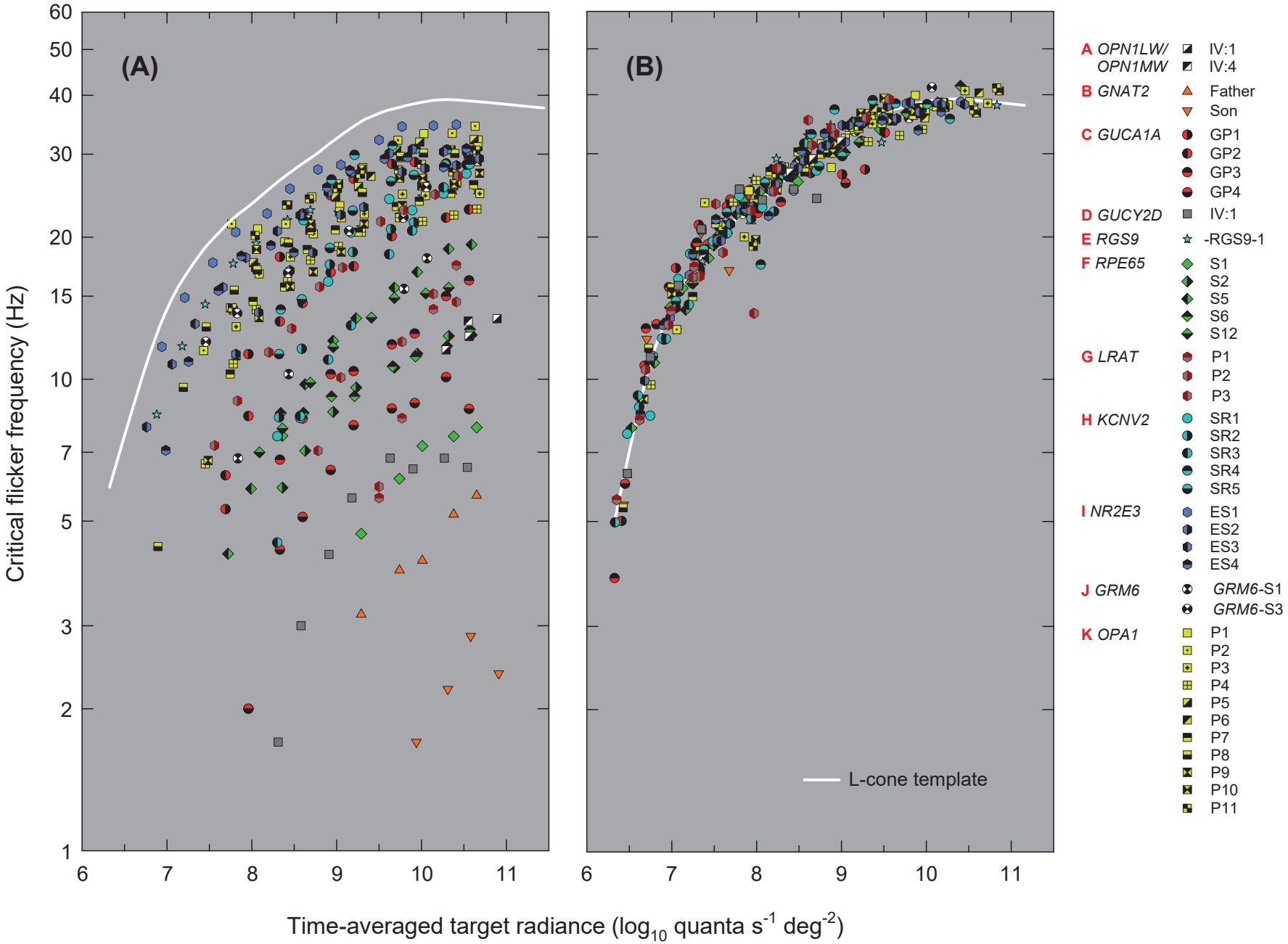
(A)
(B)
Critical flicker frequency (Hz)
60
50
40
30
20
15
10
7
5
3
2
1
6
7
8
9
10
11
Time-averaged target radiance (log10 quanta s-1 deg-2)
L-cone template
A OPN1LW/ OPN1MW
IV:1
IV:4
B GNAT2
Father
Son
C GUCA1A
GP1
GP2
GP3
GP4
D GUCY2D
IV:1
E RGS9
-RGS9-1
F RPE65
S1
S2
S5
S6
S12
G LRAT
P1
P2
P3
H KCNV2
SR1
SR2
SR3
SR4
SR5
I NR2E3
ES1
ES2
ES3
ES4
J GRM6
GRM6-S1
GRM6-S3
K OPA1
P1
P2
P3
P4
P5
P6
P7
P8
P9
P10
P11

FIGURE 10

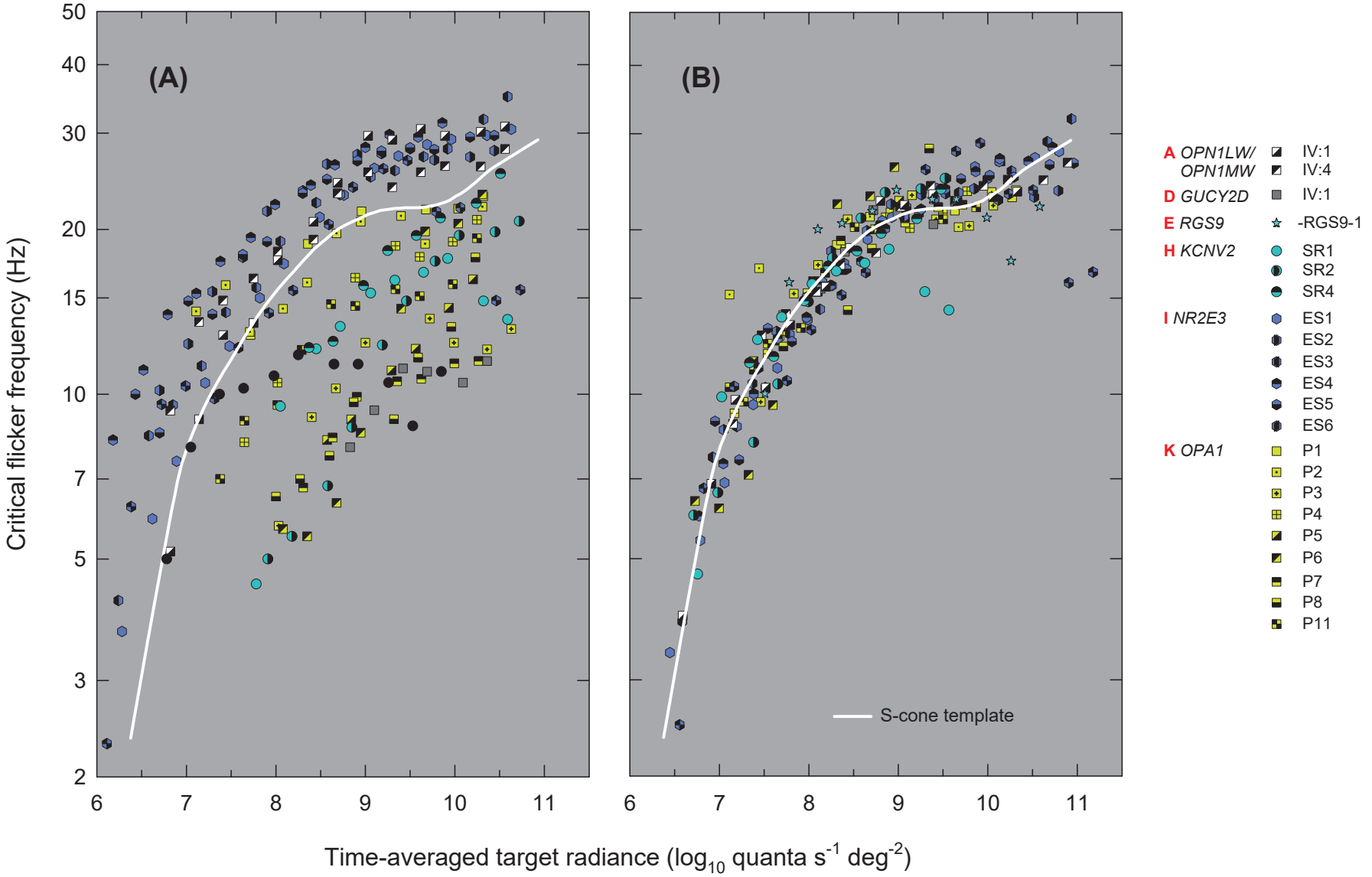
(A)
(B)
Critical flicker frequency (Hz)
50
40
30
20
15
10
7
5
3
2
6
7
8
9
10
11
Time-averaged target radiance (log10 quanta s-1 deg-2)
S-cone template
A OPN1LW/ OPN1MW
IV:1
IV:4
D GUCY2D
IV:1
E RGS9
-RGS9-1
H KCNV2
SR1
SR2
SR4
I NR2E3
ES1
ES2
ES3
ES4
ES5
ES6
K OPA1
P1
P2
P3
P4
P5
P6
P7
P8
P11

FIGURE 11

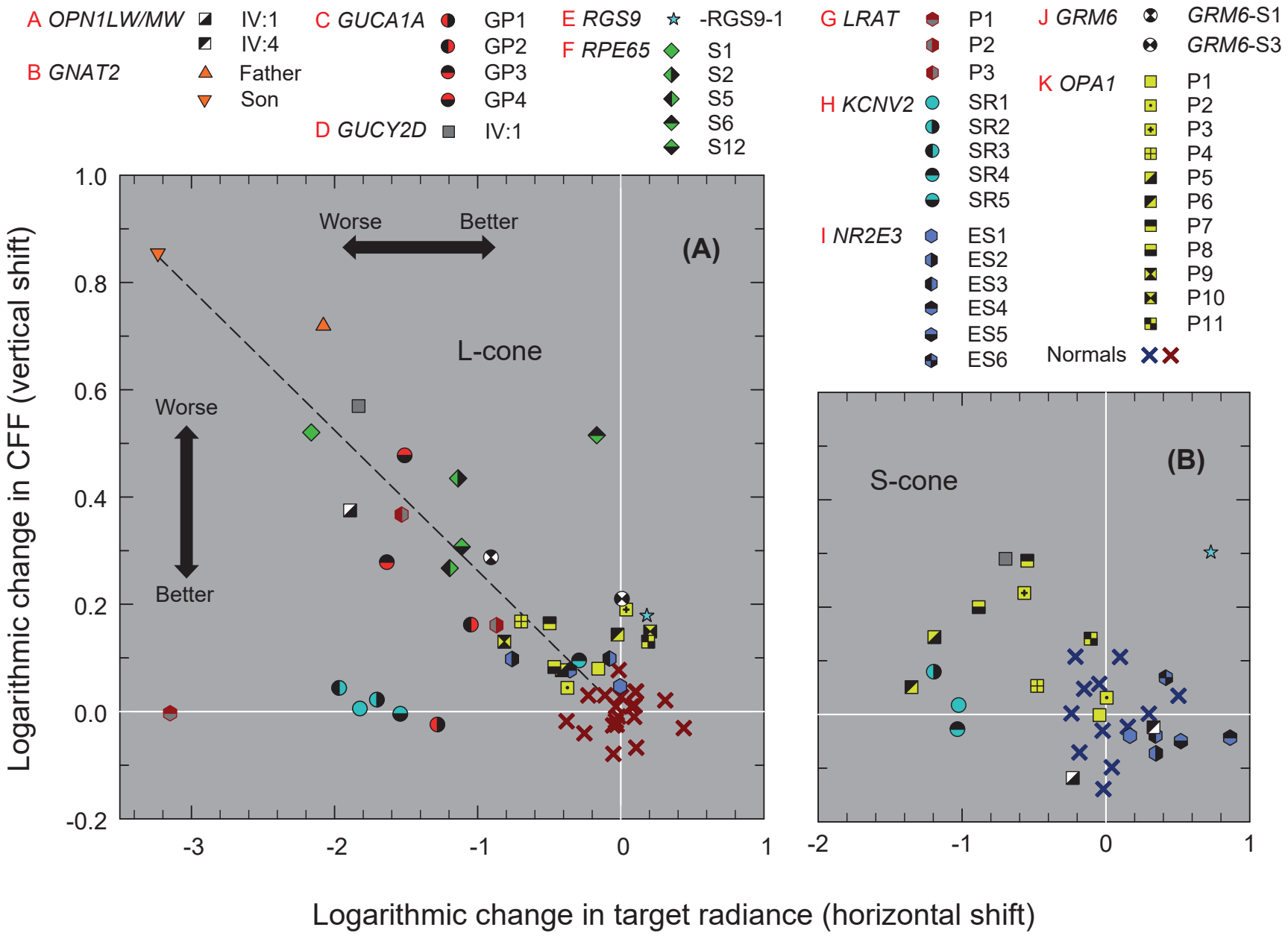
A OPN1LW/MW
IV:1
IV:4
B GNAT2
Father
Son
C GUCA1A
GP1
GP2
GP3
GP4
D GUCY2D
IV:1
E RGS9
-RGS9-1
F RPE65
S1
S2
S5
S6
S12
G LRAT
P1
P2
P3
H KCNV2
SR1
SR2
SR3
SR4
SR5
I NR2E3
ES1
ES2
ES3
ES4
ES5
ES6
J GRM6
GRM6-S1
GRM6-S3
K OPA1
P1
P2
P3
P4
P5
P6
P7
P8
P9
P10
P11
Normals
Worse
Better
(A)
L-cone
Worse
Better
(B)
S-cone
Logarithmic change in CFF (vertical shift)
Logarithmic change in target radiance (horizontal shift)
1.0
0.8
0.6
0.4
0.2
0.0
-0.2
-3
-2
-1
0
1
-2
-1
0
1